Arabian Journal of Geosciences (2023) 16:220
https://doi.org/10.1007/s12517-023-11304-5

ORIGINAL PAPER

Reappraisal of tsunami hazard for the Northern Coastal of Egypt considering sea level rise and delta subsidence scenarios

Ahmed M. O. Kamhawy[1] · Hany M. Hassan[2] · Heba M. ElKosery[2,3]

Received: 10 November 2021 / Accepted: 18 February 2023 / Published online: 4 March 2023

Abstract

In this research, we have compiled a catalogue of the worst tsunami earthquakes that caused destruction and losses in the northern coastal region of Egypt. Variability in seismic source parameters reflects the level of cognitive uncertainty that exists because most of these destructive tsunamis, if not all, occurred in the pre-instrumental period. We also synthesized a set of hypothetical tsunamis constrained by seismotectonic knowledge of the area of influence to embrace the uncertainty. We also collected the topo-bathymetry information available to make a simulation on the scale of the Egyptian north coast. The multiple scenarios were computed considering references and hypothetical scenarios, and results were presented in maps and tables for wave heights, inundation depth, and estimated arrivals. Comparisons were made between the results calculated in this study and those from previous studies. These were done to identify and measure the reasons for the difference and similarities. The results may contribute to developing risk reduction strategies and a national early warning system. Variability in tsunami intensity measures is prepared for the hypothetical scenarios due to the difference in the fault's magnitude, location, and geometry. Also, for the first time, temporally based scenarios the sea-level rise and delta sinking were considered in order to highlight the importance of multi-risk analysis for the region of interest. The insight on incorporating other hazards of the temporal resolution indicates a significant increase in inundated areas and wave height. Therefore, proper and detailed estimation of multi-hazard maps for the coastal region of the Nile Delta is highly required to protect the ongoing sustainable development and protect the people and their assets.

Keywords Tsunami hazard assessment · Variability in tsunami source parameters · Eastern Mediterranean Basin · The Nile Delta · Egypt · Sea level rise and delta sinking scenarios

Introduction

A prevalent notion among those not earthquake experts is that tsunamis are very rare in the Mediterranean Basin. Such conception could be attributed to the relatively long return period of strong earthquake-tsunami incidence or due to lack of recognition by media in present and past and culture of disfavors remembrance of past crisis. Nevertheless, close inspection of the geological, historical records and archeological pieces of evidence of tsunamis reveals that the Mediterranean's coastal communities have witnessed many tsunami impacts through the lengthy history some of them were catastrophic (Papadopoulos et al. 2007; Papadopoulos 2003). Most of those catastrophic tsunami events are well-reported and described in many historical sources written in different languages across the Mediterranean region, which constituted the foundation for publishing numerous tsunami data anthologies (e.g., parametric and descriptive catalogues, reports, and diaries).

The convergence between the Eurasian and African tectonic plates (DeMets et al. 2015) controls the spatiotemporal distribution of seismic activity in the Mediterranean Sea and adjacent regions. The relatively complex tectonic setting of the Eastern Mediterranean Basin-EMB makes it the most prone to high earthquake activity of various faulting mechanisms. Some of them can generate tsunamis of

Responsible Editor: Longjun Dong

✉ Hany M. Hassan
hany_hassan@nriag.sci.eg

[1] AIECON Consultant L.L.C, Cairo, Egypt

[2] National Research Institute of Astronomy and Geophysics, Helwan 11421, Cairo, Egypt

[3] Department of Mathematics and Geosciences, University of Trieste, Trieste, Italy

different severity levels based on earthquake magnitude and other seismological parameters (Woodward 2009). Statistically, about 9% of tsunamis worldwide have occurred in the Mediterranean Sea, where 87% were generated due to earthquakes, Atwater et al. (1999). Moreover, submarine and coastal landslides could happen in the EMB, partly due to the steep bathymetric terrain that symbolizes much of the basin.

The tsunami hazard in the Mediterranean Sea is often underestimated in the region and parts of Europe. However, many tsunamis were reported in the available catalogues, according to the most recently published tsunami catalogues; see Fig. 1. However, the past years have witnessed an increasing number of investigations dedicated to evaluating the tsunami hazard in the EMB. Still, an update must be done when new data, details, and methodology are released (Hassan et al. 2020).

The primary tsunamigenic earthquake sources in the EMB are identified by combining geological and tectonic data with historical and instrumental earthquake records (Papadopoulos et al. 2014) (Figs. 1 and 2). Consequently, the tsunamigenic earthquake sources in this region are generally subdivided by many experts into three major tsunamigenic sources, i.e., Hellenic Arc, Cyprian Arc, and Levantine Coast (Tinti et al. 2005; Yolsal & Taymaz 2010).

The 365 and 1303 CE earthquake tsunamis are the most investigated scenarios mainly due to their vast effects and well-known severity as they caused catastrophic and basin-wide impacts across the EMB. These large events are well-documented and preserved in the written historical reports, morphological, and geological traces as well (Soloviev et al. 2000; Ambraseys and Synolakis 2010; Shah-Hosseini et al. 2016; Salama et al. 2018). A recently accomplished geomorphologic study for the Egyptian coast of the Mediterranean carried out by Torab and Dalal (2015) has suggested that the presence of oriented huge boulders was deposited by either paleo-tsunami mega waves or by sea waves during winter storms. Most of those boulders were relocated from the continental shelf and scattered 90 m away from the shoreline, 4 m above the present mean sea level-MSL.

The Egyptian-Mediterranean coastal zone undergoes accelerated development and construction of new cities, infrastructure, lifelines, and critical structures to support Egypt's sustainable development goals and 2030 vision. These bring diversified opportunities and investments to the coastal zone of Egypt. However, this coastal zone faces many land and marine challenges and hazards (e.g., sea level rise, land subsidence, earthquake, tsunamis). These hazards can de-accelerate and disrupt the rate of the development or increase the future risk since more exposure is there if they are not addressed from the beginning. Therefore, the current work aims at providing a comprehensive study of tsunami hazard on the Northern coast of Egypt that jointly incorporates the tsunami hazard, the Delta subsidence, and sea level rise (SLR) scenarios in the computation of

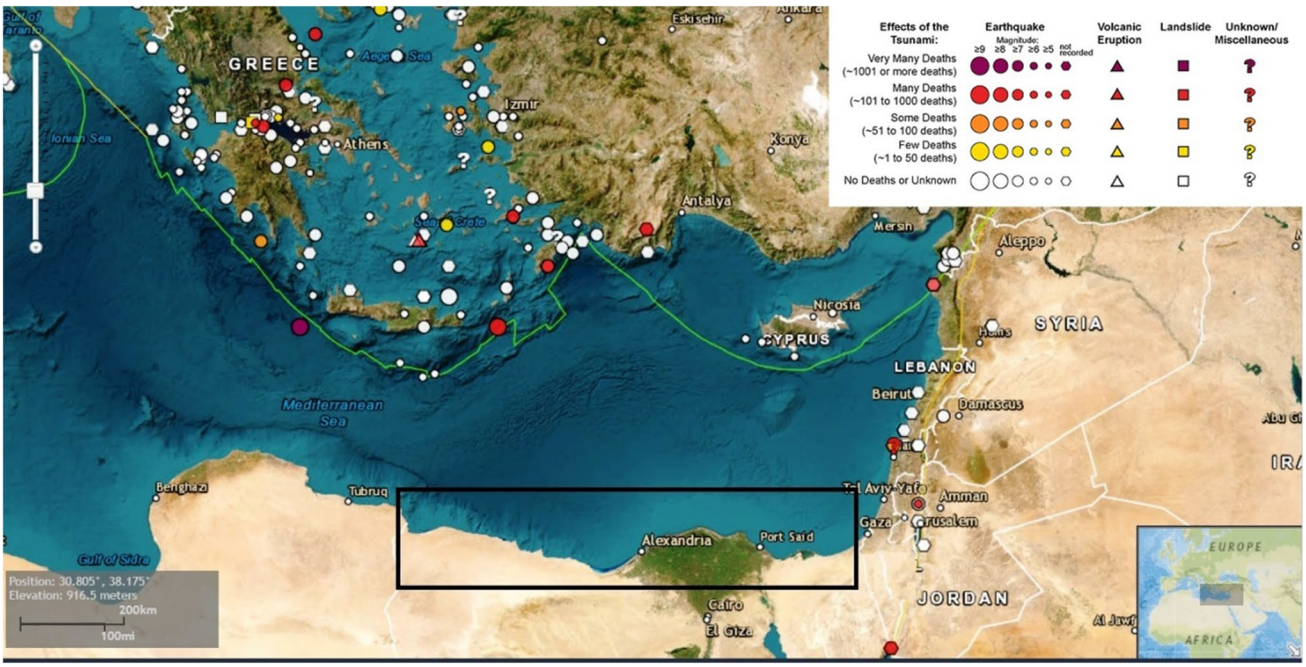

Fig. 1 Tsunami activity in the EMB (area of influence) classified as anfunction of source type, magnitude and effects where the data are extracted from National Geophysical Data Center/World Data Service (NGDC/WDS) from 2100 BCE to 2021 CE and the location of the study area, https://www.ncei.noaa.gov/maps/hazards/, last access March 2021

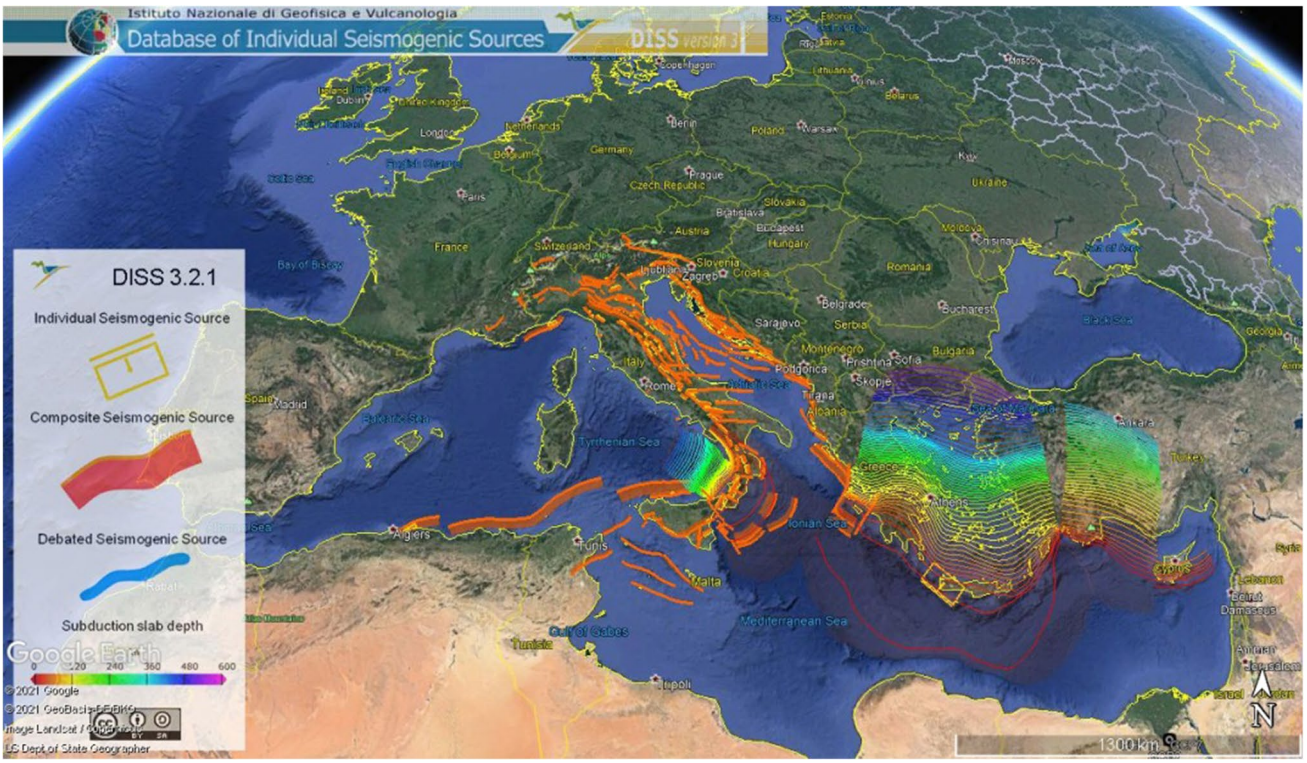

Fig. 2 Map of seismogenic zones developed for the Mediterranean Sea after DISS 3.2.1 (http://diss.rm.ingv.it/diss/, last access March 2021)

final inundation and wave height maps. However, the joint analysis and assessment of multi-hazard is indispensible for proper understanding and evaluation of the risk; this work represents a cornerstone in this track.

Different sources usually generate risks, natural (e.g., earthquake, volcano), biological (e.g., COVID-19 pandemic), and anthropogenic (e.g., Ma et al. 2018 and 2019). Each natural and anthropogenic hazard must be identified and characterized using corresponding methods (e.g., Dong et al. 2021). The scientific community has witnessed that during the current COVID-19 pandemic, a natural hazard occurred. Consequently, the reported number of casualties due to hazard impact and contiguous people due to COVID-19 are augmented. Evaluating risks related to different sources is generally done through independent analyses, adopting disparate procedures and time–space resolutions. This traditional strategy of risks evaluation has some evident and considerable weaknesses: (1) it is difficult, if not impossible, to compare risks of different origins; (2) the implicit unjustified assumption of independence of the risk sources leads to neglect of possible interactions among threats and/or "cascade" effects. In practice, this means that a potential multi-risk index could be higher than the simple aggregation of single risk indexes calculated considering each source as independent from the others. Joint analysis and quantification of all the anthropogenic and natural risks that can affect a territory (multi-risk approach) is essential for developing a sustainable environment and planning land use. In turn, these will maintain the national sustainable development planning and vision (Egypt vision 2030) during a crisis. Multi-risk evaluation is a relatively new field developed partially by experts with different backgrounds (engineering, statistics, seismology, toxicology, etc.).

In this work, we adopted a multi-scenario tsunami hazard approach that incorporates different SLR temporal-based and the Nile Delta subsidence scenarios. Therefore, we selected different tsunamigenic earthquake scenarios that vary spatially across each predefined tsunamigenic source (Figs. 1 and 2). Also, we compiled a database of fault rupture models developed by different tsunami hazard studies published in peer-reviewed journals. These models must coincide with the present-day tectonic regime of the area of influence-AOI (i.e., EMB). As an example, three different reliable tsunamigenic source models for the 365 CE tsunami are selected and adopted to model and study the variability in tsunami hazard for this individual scenario (Table 2). This represents a preliminary step toward creating a set of hypothetical scenarios to demonstrate the importance of having a range of possible results based on a comprehensive understanding of the seismogenic activity of the AOI and to present a reasonable degree of conservatism in hazard estimation.

The main outcomes of this work is to develop hazard maps based on an envelope of possible tsunami scenarios taking into consideration the uncertainty related to earthquake parameters. Via numerical simulation, an envelope of hazard levels (e.g., average, maximum) is introduced in this work to cover a broad range of plausible earthquakes, which may aid further in the following conclusions and decision-making process.

Additionally, this work includes the combined effects of other interchangeably occurring natural phenomena such as tide, storm surge, delta subsidence, and lastly, the expected future SLR in agreement with the Intergovernmental Panel on Climate Change-IPCC Fifth Assessment Report (https://www.ipcc.ch/assessment-report/ar5/). This study can be considered a fundamental attempt to study tsunami in combination with such factors to the best of our knowledge. The results of this work could raise the awareness and guide decision-makers and other potential users in the designation and development of effective mitigation strategies, evacuation planning, and even a national warning system.

Socio-economic aspects of the study region

Egyptian-Mediterranean coastal zone has many economic and environmental opportunities and resources that attract the attention of investors and stakeholders. Egypt is densely inhabited among all North African countries; the country's population has surpassed 100 million. The excellent climate and sandy beaches that characterize this coastal zone is the main drive of investors and tourists attraction. The blue economy provides many jobs and opportunities for coastal communities and trade routes and ports as Egyptian maritime play a vital role in the global trade network. It is worth noting that unplanned urban development negatively affects the sustainability of development planning and environmental defenses because of the aggressive actions against the existing natural-based mitigation measures.

The Nile Delta occupies the Northern middle part of Egypt. It extends from Cairo in the south, where the Nile River divides into two main branches (i.e., Rosetta and Damietta) till the Mediterranean coast, in which they drain. Egypt's Nile Delta and northern coastline have been recognized as vulnerable to impacts of SLR (CORI 1992; El-Raey et al. 1997). It should be mentioned that the Nile Delta region is characterized by two very notable characterizations; it has a flat low elevation terrain and has a very high population density (Fig. 3). These characters may make it the most vulnerable and risky place in the area of interest. Truthfully, socio-economic and environmental impacts on the Nile Delta became Egypt's primary concerns; nevertheless, a substantial increase in sea level could endanger the livelihood of millions of Egyptians before the end of the twenty-first century, as per the testimony of Egyptian environmental authorities.

The coastal area of the Nile Delta of Egypt faces many risks that may challenge the stability of the related social, economic, and environmental systems (El-Raey 2010). In

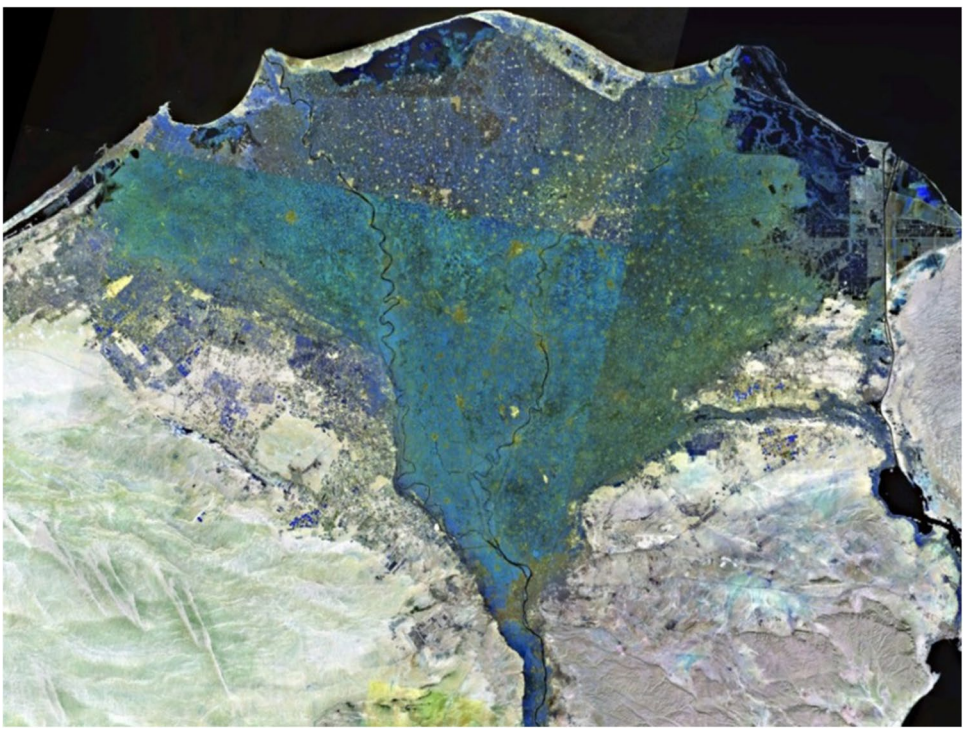

Fig. 3 Satellite image of the Nile Delta region (Captured and cropped from NASA World Wind)

particular, it faces natural hazards from both the sea and the land and a combination of possible cascading risks, so a multi-risk approach is needed, integrating data and methodologies from various disciplines, including exposure and vulnerability of community, physical system, and environment. These risks can be mitigated if adequate proactive preparedness and mitigation actions are taken (Fig. 3).

Farmers within the Nile Delta region face considerable crop production losses each year due to the combined action of the rising water table and saline seawater intrusion, which renders the soil infertile (El-Raey 2010). This fact is particularly worrying given that nearly half of Egypt's crops such as corn, rice, cotton, and wheat are grown in the delta region (Abdelaal & Thilmany 2019).

Methodology

In this section, we describe the implemented workflow in the current study. Then we computed reference runs to compare the results with those published as the first stage of this work and to incorporate the variability in the source model and investigate their effects on the final results. It is noteworthy to mention that an integral part of this study is to identify and evaluate the uncertainty associated with the necessary descriptive parameters of the past earthquake and the mere fact that earthquakes rarely (if ever) occur the exact way twice. Firstly, we collected necessary input data and pre-processing them. The tsunamigenic earthquake source parameters are collected from two primary sources: (a) published earthquake catalogues, (b) previous tsunami hazard studies. Moreover, we briefly explained the numerical models used to model tsunami waves generation, propagation, and inundation. Essential components needed to carry out tsunami simulation are as follows:

- Bathymetric and topographic maps for the study area.
- Descriptive parameters of tsunamigenic earthquakes.
- Numerical models.

Each of these components is discussed below as follows.

Bathymetric and topographic maps

The National Oceanic and Atmospheric Administration has developed a set of bathymetric grids utilizing available sounding data and the global marine gravity model to construct bathymetric grids. These grids have 30 and 15 arc second resolutions (1000 m and 500 m, respectively), namely the SRTM_30 PLUS (Weatherall 2009) and the SRTM_15 PLUS released in 2014, Becker et al. (2009). Land topography data are available free access from SRTM ASTER digital elevation models.

We employed two nested grids to simulate tsunami generation, propagation, and inundation in the deep ocean and across the Egyptian coastal area. The coarser mesh size (Grid A) of 500 m is used for the deep sea condition (Fig. 4). In addition, a more satisfactory resolution grid of 250 m (Grid B) is utilized for the near coastal area of the Mediterranean Sea (Fig. 4) to count for the wave arrival and possible modifications and the inundation calculation. Both mesh sizes agree with the Pacific Marine Environmental

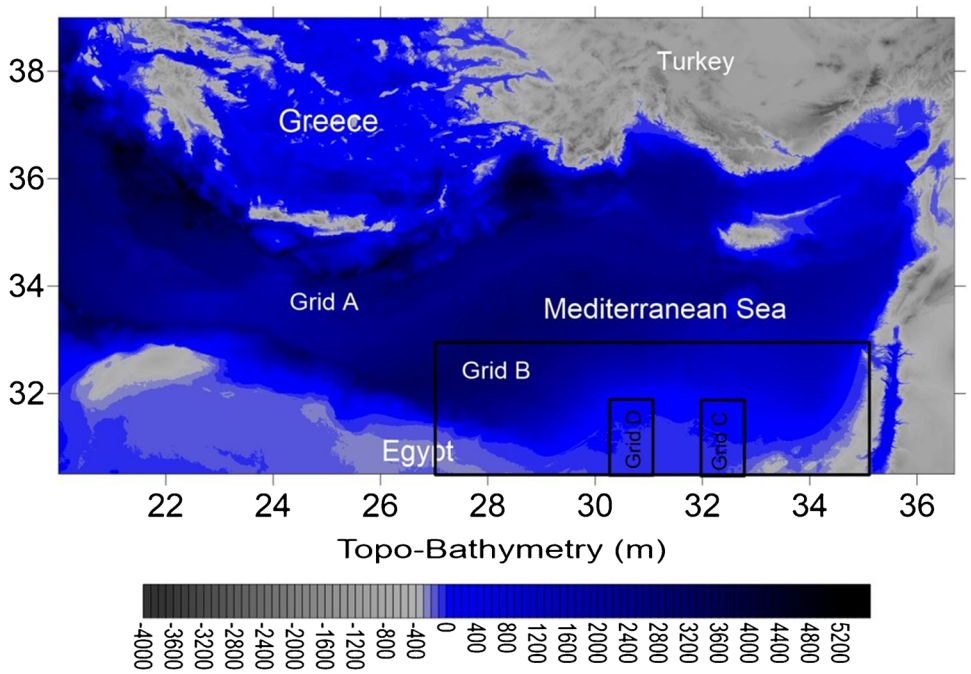

Fig. 4 Topographic-bathymetry domain grids of the areas of interest and influence being utilized in tsunami simulation

Laboratory-PMEL recommendations (Freitag et al. 2006); see Fig. 4. Both grids implement the UTM coordinate system (Universal Transverse Mercator) and use the WGS84 datum. Moreover, the SRTM_15 PLUS and ASTER GDEM were utilized to derive smaller 90-m resolution grids for the Suez Canal regions by Grid C (Fig. 4) and the Rosetta promontory represented by Grid D (Fig. 4). This was done in order to compute detailed inundation maps for these two selected areas due to their importance and presence of dense economic and sociological activities (Table 1).

Compilation and selection of tsunamigenic earthquake scenarios

The fundamental problem is that we still do not know precisely where and when the subsequent earthquakes will happen. In particular, we are regularly reminded that where and when large earthquakes happen is more variable than we expected. Given the short instrumental seismological history, it is not clear how to estimate how often the biggest, rarest, and potentially most destructive earthquakes like the 2011 Tohoku one will happen. We may never figure out things, notably how to predict when big earthquakes will occur on any time scale shorter than decades.

The most traditional approach in tsunami hazard assessment and designation of mitigation measures is utilizing a single earthquake scenario per each tsunamigenic earthquake source deduced based on multidisciplinary investigation for historical events. Therefore, tsunami hazard analysts may encounter several hypothetical scenarios based on available information that continuously updates with augmentation in observation and methods. This fact reflects the endemic lack of knowledge regarding the location, depth, fault configuration, and magnitude of the faults on which these tsunamigenic earthquakes happened.

In tsunami hazard assessment, a quite clear observation is that we lack complete and accurate information. We thus need to decide what to do given these uncertainties. Therefore, besides considering other geo-hazards, variability in fault rupture parameters is considered in hypothetical scenarios. Moreover, to be prepared for the extreme event and embrace uncertainty, the Maximum Credible Earthquake scenarios (= magnitude of historical event + 0.5) is adopted for each tsunamigenic source in the EMB, i.e., the area of influence. This work considers variations in fault rupture parameters and the magnitude of maximum credible earthquake (MCE). The variability in the rupture parameters is constrained based on the understanding obtained from the tectonic setting and findings from recent instrumental earthquake investigations. MCE's magnitude M_{design} can be tentatively and, until proven otherwise, set equal to the maximum, historical or instrumental, observed magnitude (M_{max}) plus 0.5 (Rugarli et al. 2019; Panza & Bela 2020).

Any attempt to assess tsunami hazard for a particular coastal region starts with gathering information on past events in the area of influence. The compilation and update efforts of complete, long, accurate, and homogeneous tsunamigenic earthquake catalogue for the EMB as much as possible have begun since several decades and still going on (Galanopoulos 1960; Ambraseys 1962; Antonopoulos 1979; Papadopoulos & Chalkis 1984; Tinti and Maramai 1996; Soloviev et al. 2000; Papadopoulos & Fokaefs 2005; TRANSFER project 2009 (Tsunami Risk and Strategies For the European Region); Ambraseys and Synolakis 2010; Papadopoulos et al. 2014). These tsunami catalogues were revisited several times by experts with the latest findings from in the historical documents, field surveys, newly uncovered geological evidence, and paleotsunami studies, e.g., Salama et al. (2018) and Papadopoulos et al. (2014). A list of well-known confirmed large tsunamigenic earthquakes in the area of influence (i.e., EMB) is listed in Table 2. The epicenter coordinates, fault rupture parameters, and the magnitude of those earthquake tsunamis have been taken from international data sources and published catalogues (e.g., Papadopoulos and Chalkis 1984; Ben-Menahem's 1979).

In this section, among many tsunamis that happened registered in human and geologic records, we describe the selected and adopted earthquake scenarios available in literature and tsunami catalogues. The selection of tsunamigenic earthquake scenarios is based on criteria and terms, which we considered a quality control criteria, i.e., (1) tsunamigenic earthquakes of reliability score equal or less than two have been removed, and (2) all tsunamis caused by reasons other than earthquake or a combination of earthquake and landslide have been eliminated.

The selected tsunami scenarios have quite enough reliability, and their impacts on the northern Egyptian coastline have been confirmed by many publications, i.e., 142, 365, 551, 1222, 1303, and 1481 CE.

The development of a consistent database of past tsunamis is of high priority for various tsunami investigations such as numerical modeling, hazard assessment, risk evaluation, raising public awareness, and deployment of tsunami warning systems. Statistical analysis of the developed earthquake tsunamis database reveals that the

Table 1 Four nested grids adopted in tsunami hazard analysis

Grid	Mesh size (m)
A	500×500
B	250×250
C (the Suez Canal)	90×90
D (Rosetta promontory)	90×90

Table 2 The EMB tsunamigenic earthquake scenarios investigated previously

Year	Lat	Lon	Length (km)	Width (km)	Focal depth (km)	Vertical disp. (m)	Strike angle (θ)	Dip angle (λ)	Rake (δ)	M_w	Event validity*	Reference
142	35.5	28.6	190.0	90.0	7.5	5.0	235.0	20	90	8.4	4	Mitsoudis et al. (2012)
365	35.0	23.0	105.0	100.0	70.0	16.0	292.5	40	70	8.5	4	Hamouda (2010a)
	35.0	23.0	233.0	38.0	15.0	12.0	312.0	20	90	8.5		Hamouda (2010b)
	35.0	23.0	100.0	90.0	10**d**	20.0	315.0	30	90	8.4		Valle et al. (2014)
551	34.0	35.5	80.0	30.0	5.0	4.0	115.0	30	90	7.5	3	Hamouda (2010b)
1222	34.5	32.5	80.0	30.0	15.0	3.0	305.0	35	110	7.8	4	
	VAR		80 **a**	50 **b**	7.5	7.5–15	235.0	20	90	8.5		Valle et al. (2014)
	VAR		50 **c**	50**b**	10.0	5–11	315.0	20	90	8.4		
1303	35.0	27.0	60.0	30.0	3.0	4.0	80.0	25	90	7.8	4	Hamouda (2006)
	35.5	28.4	190.0	35.0	10	5.0	300.0	20	90	8.1		Tinti et al. (2005)
	34.0	26.0	190.0	35.0	20.0	8.0	300.0	45	90	8		Hamouda (2010b)
	34.0	28.0	122.5	32.5	15.0	6.0	67.0	48	-34	7.3		El-Sayed et al. (2000)
1481	36.5	28.3	110.0	35.0	12.0	5.0	300.0	20	90	7.1	**4**	Papadopoulos et al. (2007)
	35.5	28.2	140.0	70.0	10.0	4.0	235.0	20	90	8.0		Hamouda (2010b)

*Based on a five points scale followed by National Oceanic and Atmospheric Administration (NOAA), 4 = definite tsunami, 3 = probable tsunami, 2 = questionable tsunami, 1 = very doubtful tsunami, 0 = event that only caused a seiche

number of remarkable tsunami events with an intensity score ≥ 9 is five in the last 700 years. As a result, as a rough estimation, a powerful tsunami is anticipated every 140 years in the EMB, on average, assuming that all historical documents are complete for at minimum the last 700 years.

Coastal hazards that threat the northern coast of Egypt

The effect of SLR, Delta subsidence, storm surge, and tides have been discussed separately in many papers, but never combined with tsunami hazard till today, according to our knowledge. Nevertheless, incorporation of these hazards may significantly affect wave height and inundation. It is worth noting that the combined effects of natural phenomena such as tide, storm surge, Nile Delta subsidence, and SLR are accounted for in our scenarios by modifying the original topographic/bathymetric grids. The relative SLR at a specific point in space and at a particular time is determined by global SLR (Eustatic changes in sea level), land subsidence, and gross accretion of fluvial sediment as indicated by Ericson et al. (2006). We combined the sea-level rise scenario in the tsunami modeling and how the SLR coupled with the delta subsidence is computed as below in Eq. 1 then added to topo-bathymetry data for joining scenarios of tsunami and SLR, which in turn modified the shoreline, bathymetry, and so inundation.

Therefore, expected relative SLR at any site for a given period can be predicted according to the following equation:

$$R_{SLR} = G_{SLR} + (V \times T) - S \quad (1)$$

where R_{SLR} is the relative sea level rise, G_{SLR} is the global SLR, V is the annual rate of land subsidence, T is the period of the scenario, and S is the gross accretion of fluvial sediments. Therefore, we consider this work as a preliminary step in the multi-hazard analysis for the Mediterranean coastal region of Egypt. The motivation behind this approach stems from the necessity of having dynamic tsunami hazard maps that consider other hazards phenomena since they can change the pattern of the hazard maps, therefore risk. Risk and resilience assessment solutions, studies, and outputs should support long-term multi-hazard management strategies (e.g., climate adaptation, disaster risk reduction and prevention and mitigation strategies), particularly for the most vulnerable regions such as the Nile Delta. To achieve that, novel interdisciplinary risk approaches to assessing human-hazard interactions and reaching the most vulnerable segments of the community. The following section shall guide the reader through the background of each component of other hazards that challenges the sustainable development plans across coastal areas of Egypt.

Sea level rise

The Egyptian National Coastal Research Institute assembled records extracted from three monitoring stations to quantify SLR. These monitoring stations are located in Port Said, Alexandria, and Burg Al-Burullus. The measurements show a SLR rate of 5.3 mm/year for Port Said, 1.6 mm/year for Alexandria, and 2.3 mm/year for Burg Al-Burullus, the Egyptian Environmental Affairs Agency in 2008 (Jol et al. 2009). The net rise in sea levels is 1.2 mm/year in Alexandria, 1.2 mm/year in Burg Al-Burullus, and 1.95 mm/year in Port Said. By 2025, approximately 200 km^2 stretch of the Egyptian coastline may be flooded due to 30 cm of SLR (Jol et al. 2009). However, the flood extent can be reduced if the decision-makers consider effective and proactive mitigation measures or decreased SLR rate.

Shaltout et al. (2015) have studied the variation in sea level using 21 years (1993–2014) of satellite altimetry data, represented by dynamic topography (DT) and examined them considering tide-gauge observations. They concluded that the sea level has been augmented by an average of 3.1 cm/decade and shows a noticeable yearly sea-level variation of 8 to 17 cm. The estimated potential

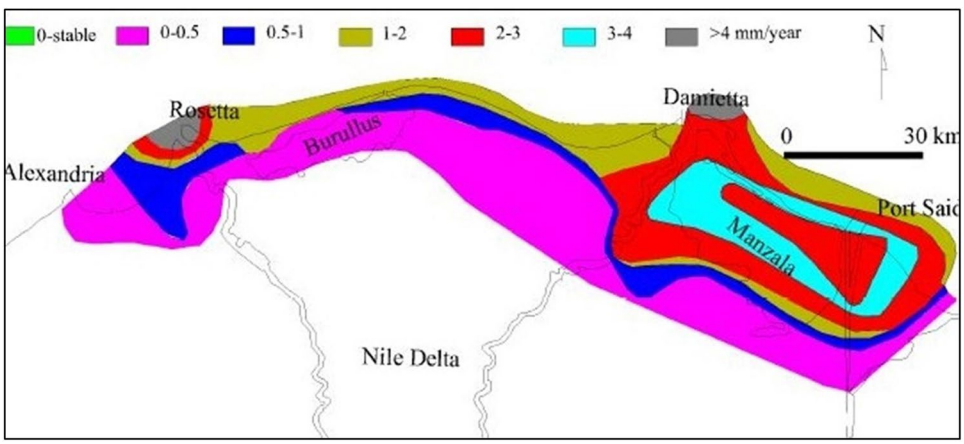

Fig. 5 Land subsidence rate north the Nile Delta after Stanley (1990)

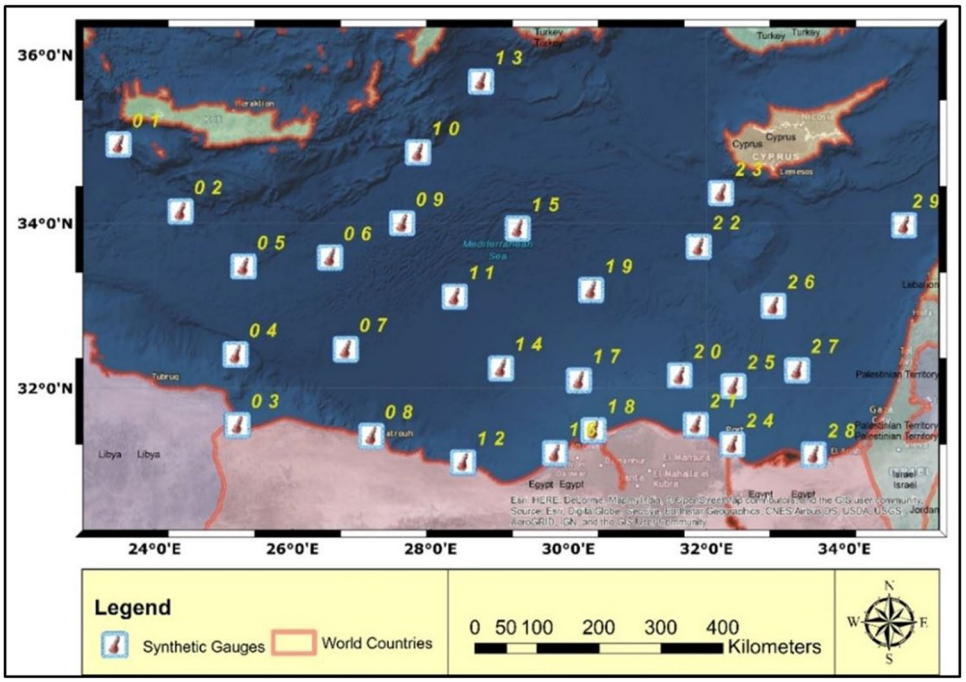

Fig. 6 Spatial distribution of synthetic tide gauges installed within the areas of influence and interest

uncertainty for the study area is defined to be ranging between 4 and 22 cm by the year 2100. The results indicate the need for effective adaptation methods to counterbalance the SLRs to protect Egypt's northern coast from flooding by 2100 (Shaltout et al. 2015).

Land subsidence

Rates of subsidence along the Nile Delta were appraised and found to be diverse widely in different areas ranging between 0.5 and 4.5 mm/year (Warne & Stanley 1993). Maximum subsidence values were located near coastal lagoons such as Manzalah Lake and around Damietta and Rosetta promontories (Becker and Sultan 2009). Severe erosion and subsidence along the Nile Delta occur after constructing barrages and dams along the main alignment of the Nile River (Frihy et al. 2010). Further adding to the problem is the drying of marshlands, which happens because of expansion works for agricultural production purposes (El-Asmar and Hereher 2011; Masria et al. 2016); see Fig. 5.

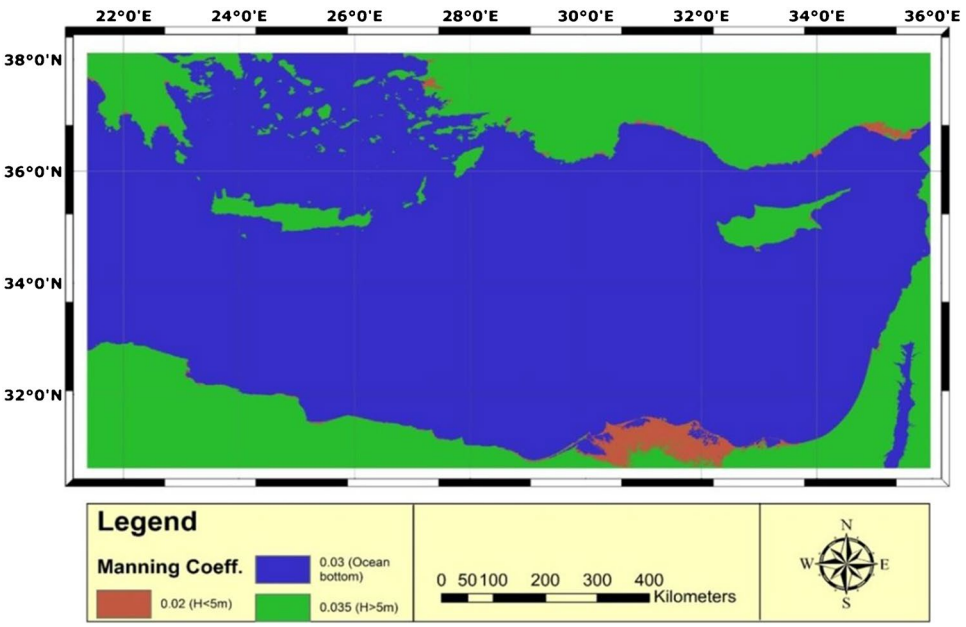

Fig. 7 Spatially variable roughness coefficients used in tsunami modeling

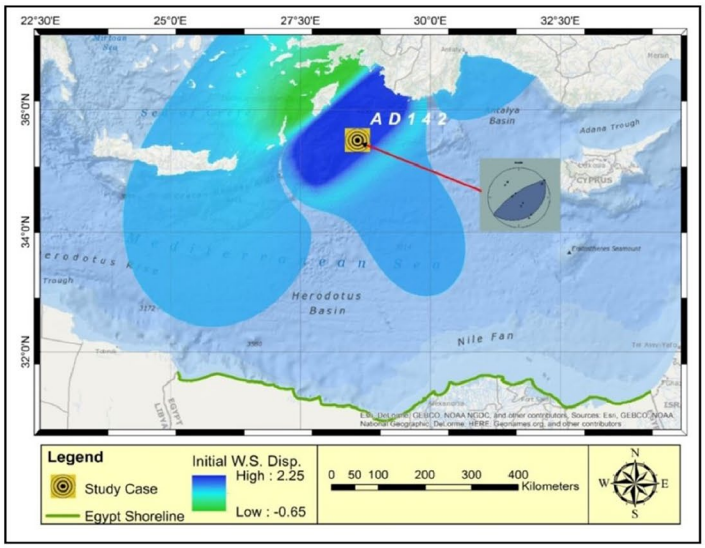

a

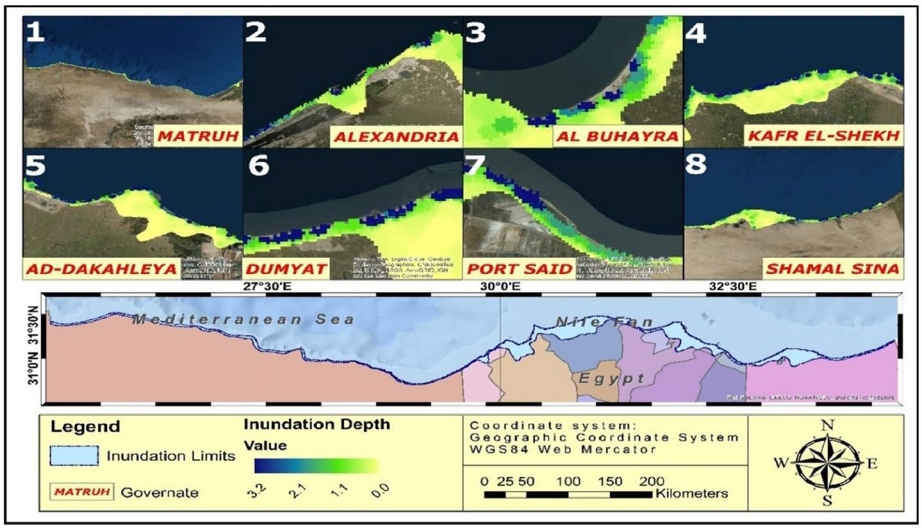

b

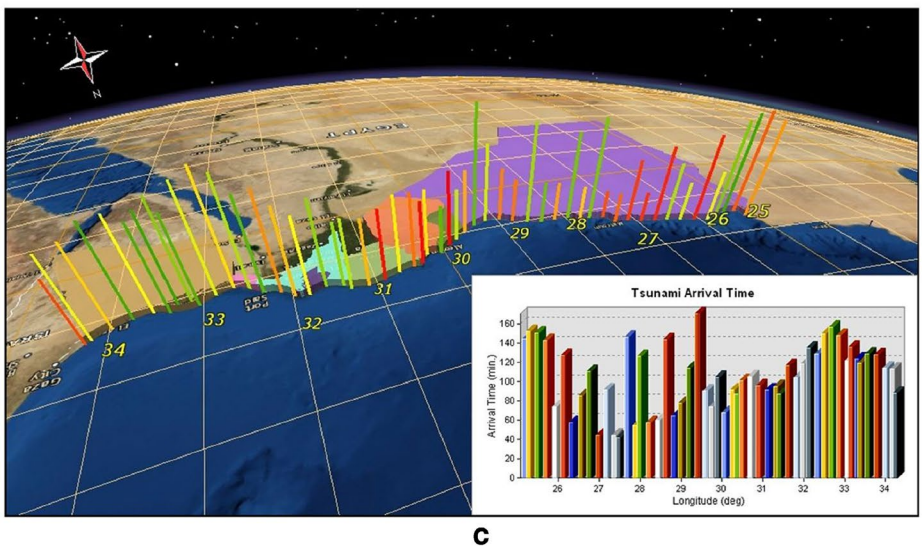

c

Fig. 8 **a** Source location and representative focal mechanism solution of the 142 tsunamigenic earthquake scenario and correspondent initial water surface displacement. **b** Maximum tsunami inundation depth along the coastal governorates estimated considering the 142 tsunamigenic earthquake scenario. **c** The distribution of ETAs along the coastline for the 142 tsunamigenic earthquake scenario. **d** Maximum tsunami wave height distribution along the coastline as a result of the 142 tsunamigenic earthquake scenario. **e** Mareograms computed at entrance of the Rosetta promontory for the 142 tsunami scenario (Top). Bottom: inundation depth (left)—maximum tsunami wave velocity (right) for the Rosetta promontory. **f** Top: mareograms computed at entrance of the Suez Canal for the 142 tsunami scenario. Bottom: inundation depth (left)-wave max. Maximum tsunami wave velocity (right) for the Suez Canal

Fig. 8 (continued)

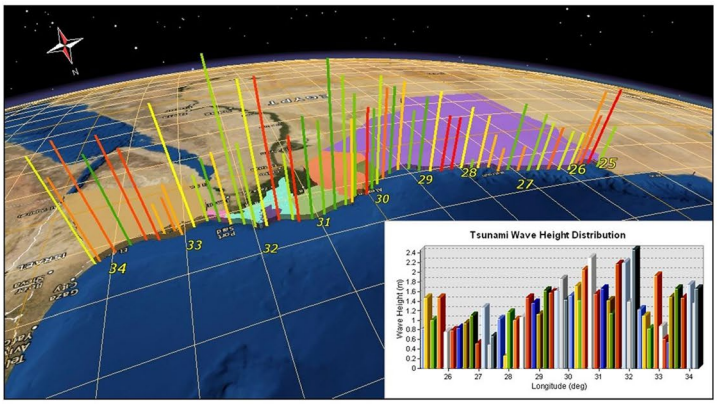

d

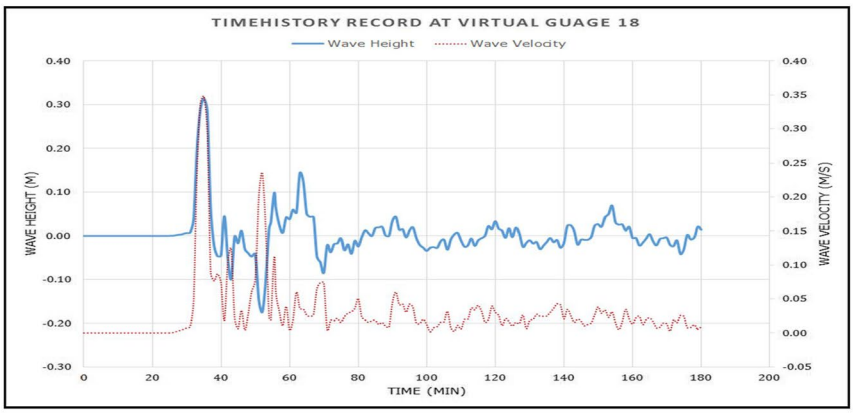

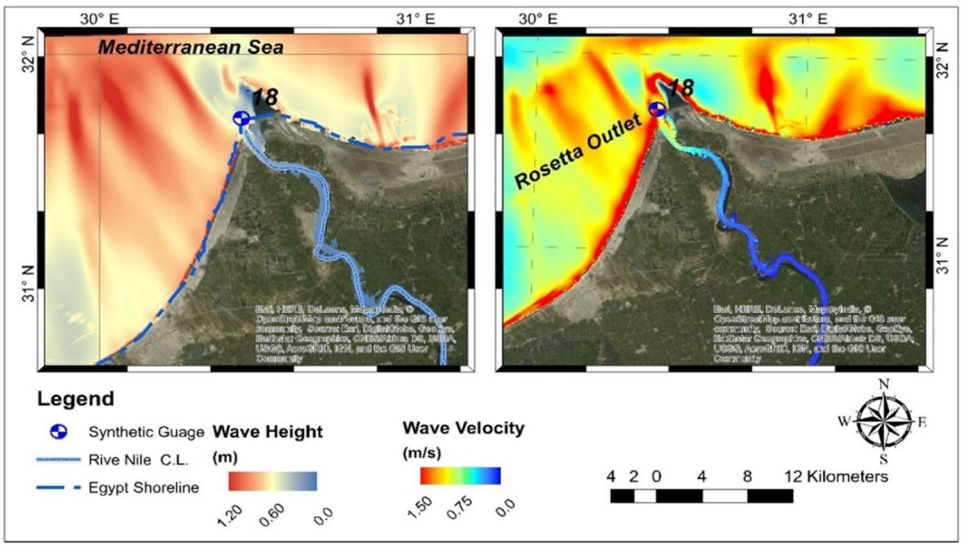

e

Numerical simulation

Due to the technological advances in the computational capacity of modern computers, it has become relevantly easier to model such a complex phenomenon. Stage one is excitation, in which we investigate the source that caused vertical disturbance to the water surface and then simulate the wave propagation until it reaches the coastline only; the third and final phase is tsunami wave inundation.

Simulation code

Two simulation codes are utilized within this work as a compromise. The NAMI DANCE code simulates all reference

Fig. 8 (continued)

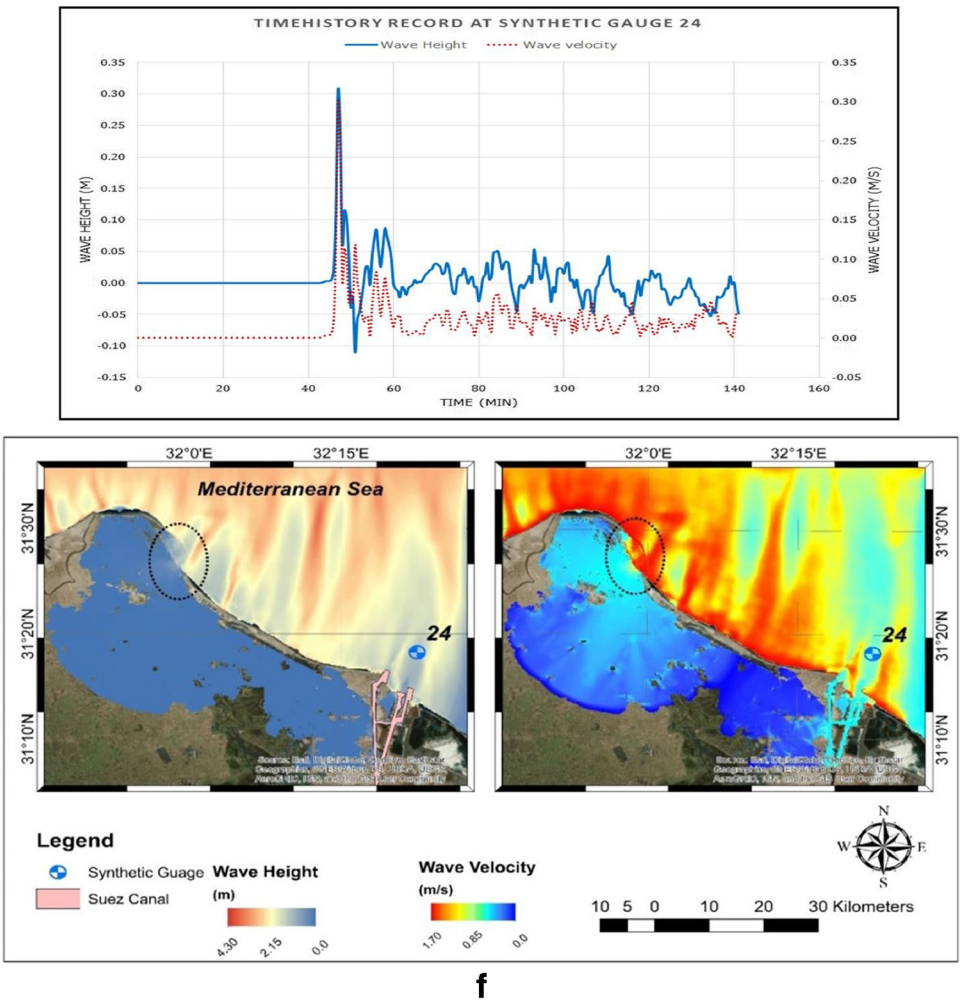

f

and hypothetical models because it is computationally less expensive. Reference tsunami source model was developed in previous studies and modeled in adopting newly released information. These models incorporate variability in the earthquake source configuration set in this work. Meanwhile, the COMCOT code is utilized for a smaller, more detailed domain as it is computationally costly, i.e., tsunami wave intrusion into the Nile River and the Suez Canal. Twenty-nine virtual tide gauges are distributed throughout the bathymetry grid of domain A to extract synthetic mareograms at selected sites. Two of these gauges are utilized as input to the COMCOT for detailed inundation studies at two locations of interest along the study area (i.e., the Rosetta promontory and the Suez Canal); see Fig. 6. Both codes use the same numerical scheme and non-linear shallow water equations with a chosen simulation time of 180 min to have enough windows for tsunami propagation/inundation sufficient to extract required tsunami intensity measures.

Table 3 Tsunami intensity measures computed for the 142 scenario at different localities

Parameter	Range value	Governorate							
		Matrouh	Alexandria	El-Beheira	Kafr El-Sheikh	Dakahliya	Damietta	Port Said	North Sinai
ETA (min)	Max	150	94	89	137	134	114	152	155
	Min	49	68	81	86	100	105	134	107
Wave Height (m)	Max	1.65	1.54	1.49	2.28	1.75	2.28	1.24	1.53
	Min	0.55	1.45	0.63	0.43	1.21	1.29	0.52	0.58
Inundation Depth (m)	Max	1.66	1.19	1.97	1.63	1.68	0.84	1.25	1.02
	Min	0.09	0.24	0.28	0.5	0.84	0.42	0.28	0.25

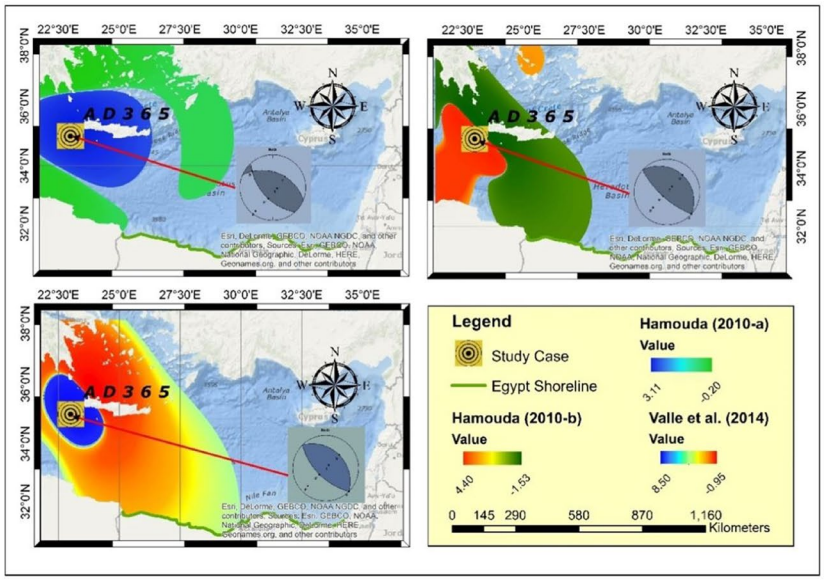

a

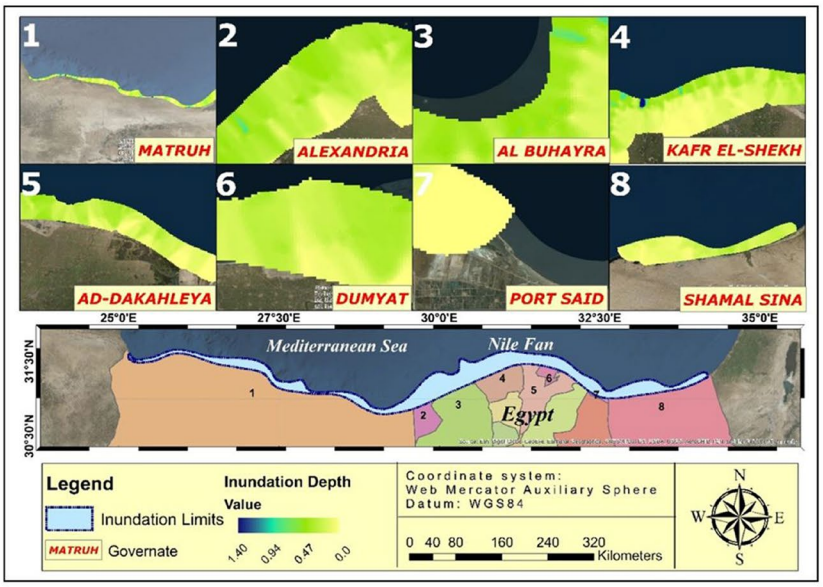

b

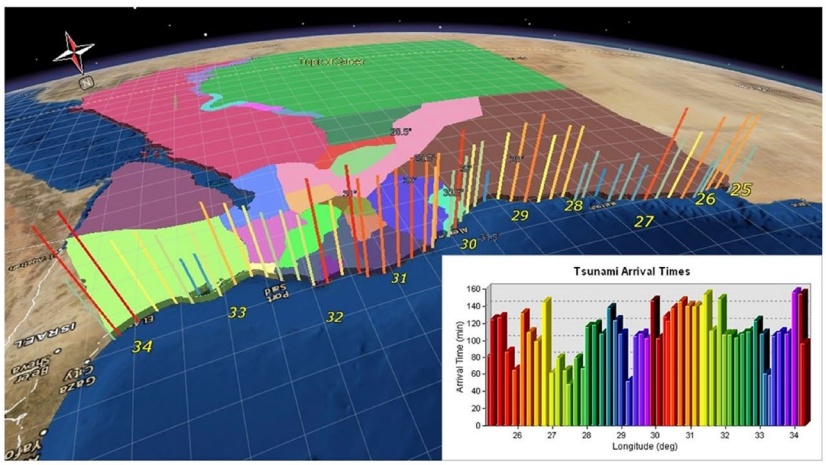

c

Fig. 9 **a** Source location and representative focal mechanism solutions for three tsunamigenic earthquake scenarios of the 365 tsunamigenic earthquake and correspondent initial water surface displacements. **b** Maximum tsunami inundation depth map considering the 365 tsunami scenarios. **c** The average ETAs distribution along the northern coastline of Egypt defined for 3 tsunamigenic earthquake scenarios of the 365 tsunami. **d** Maximum tsunami wave height distribution along the northern coastline of Egypt defined for three different scenarios of the 365 tsunamigenic earthquake. **e** Top: Mareograms computed at entrance of the Rosetta Barrage correspondent to the 1303 tsunami scenario. Bottom: inundation depth (left)—maximum tsunami wave velocity (right) for the Rosetta promontory. **f** Top: mareograms computed at entrance of the Suez Canal for 365 tsunami scenario. Bottom: Inundation depth (left)-wave max. Maximum tsunami wave velocity (Right) for the Suez Canal. **g** Comparison of arrival times between the current study for the 365 tsunami and Hamouda 2010a and b (top), comparison of inundation depths (bottom)

Fig. 9 (continued)

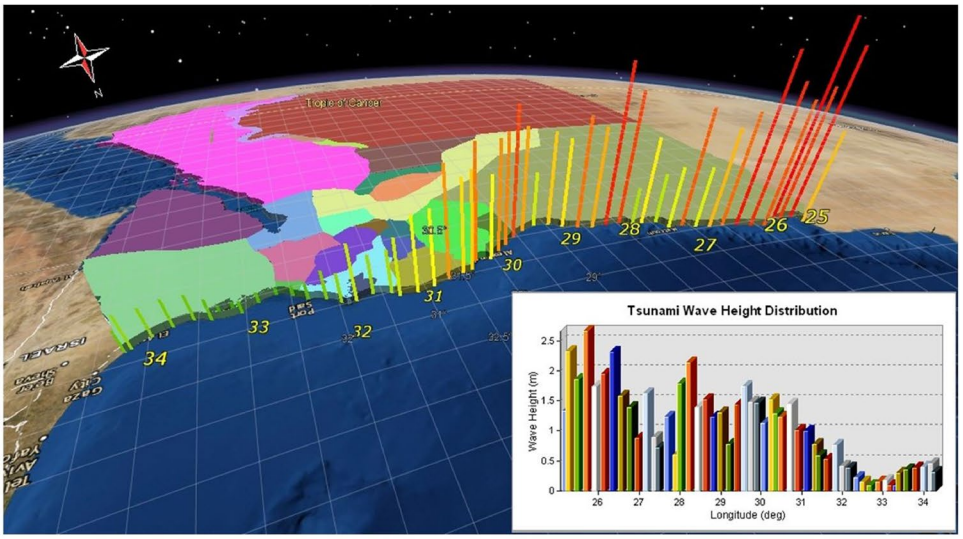

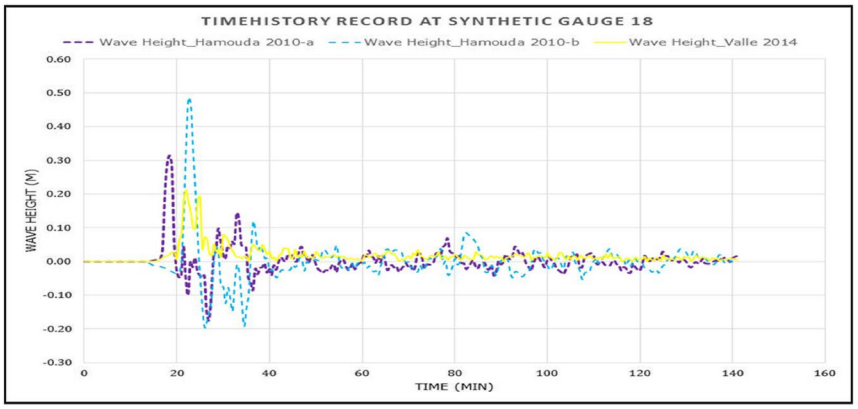

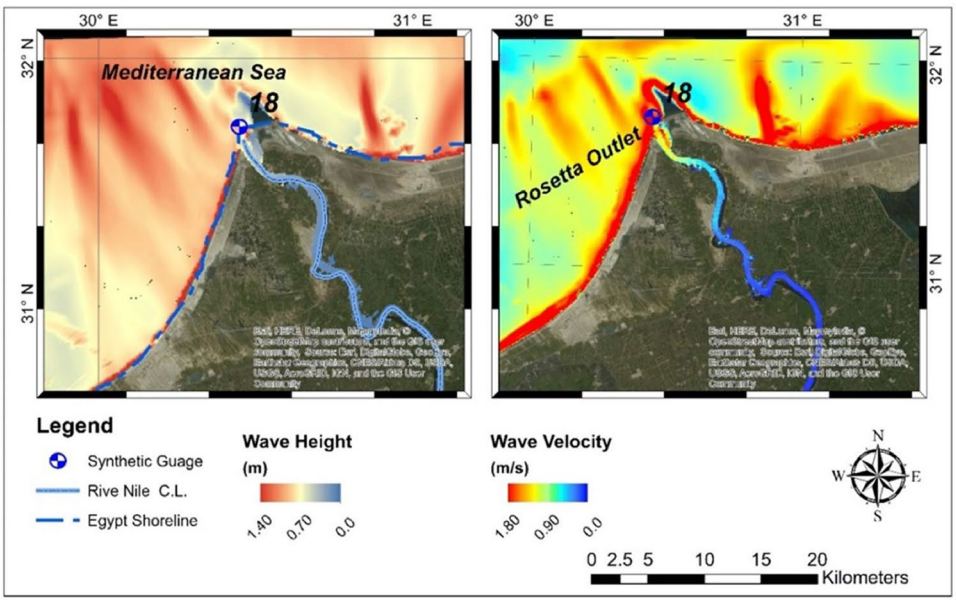

Fig. 9 (continued)

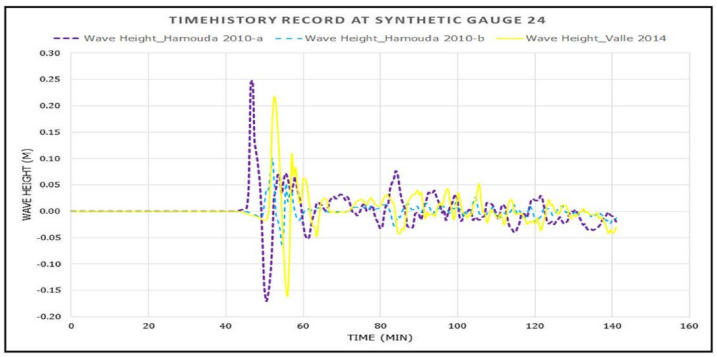

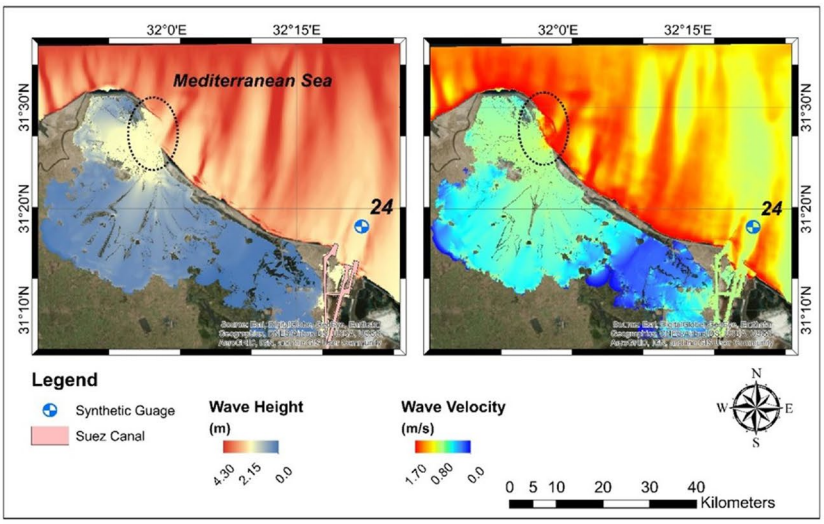

f

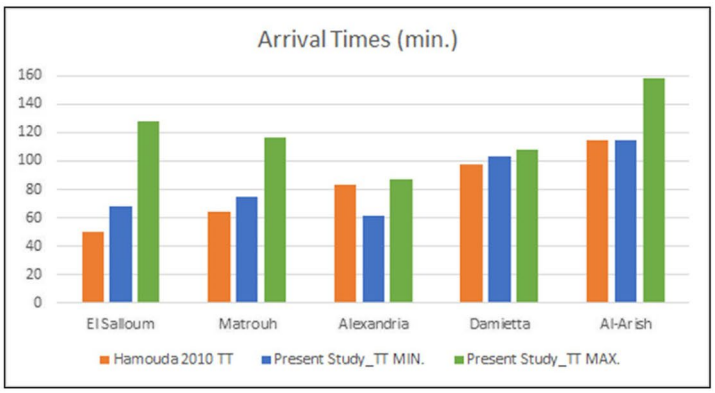

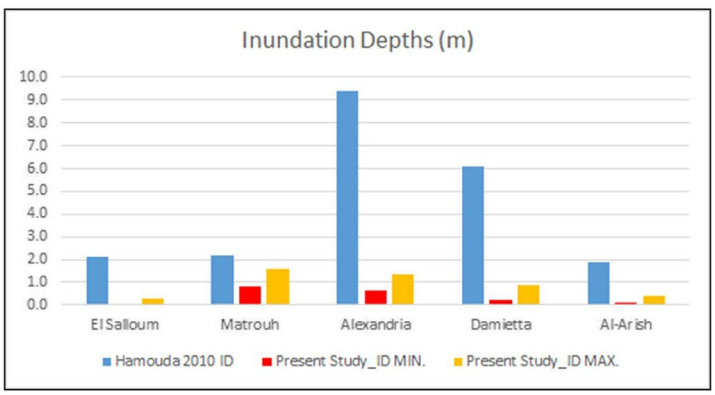

g

NAMI DANCE is a computational tool that provides direct simulation and dynamic visualization of tsunamis to the user and for assessment, understanding, and investigation of tsunami generation and propagation mechanisms. It is developed in C++programming language by following leapfrog scheme numerical solution procedures proposed by Shuto et al. (1990) and Shuto et al. (1991). Also, it has several modules for the development of all requirements, in addition to necessary tsunami parameters, Yalciner et al. (2006, 2010) and Zaytsev et al. (2019).

COMCOT is the abbreviation of the Cornell Multi-Grid Coupled Tsunami model. This tsunami modeling package is developed to study the entire lifespan, including its generation, propagation, and inundation. The model uses a modified leap-frog finite difference scheme to solve shallow water equations in both Spherical and Cartesian Coordinates. A two-way nested grid algorithm, dynamically coupled up to multiple levels, is implemented in the model to account for the variation of length scales of tsunami during its evolutions in different regions. Various tsunami generation mechanisms have also been developed to investigate tsunamis from various sources, Wang and Power (2011).

Three different values of Manning's roughness (n) are adopted for tsunami hazard computation for the area of influence (offshore) and area of interest (coastal area), Chow (1960) as shown in Fig. 7. This figure shows variation in assigned Manning values across the computational domain.

Results and discussion

This section presents the results of tsunami modeling of reference tsunamigenic earthquake scenarios listed in Table 2. The hypothetical scenarios are listed in Tables 11 to 13 and their potential impact on the Egyptian coastline is duly discussed. More than 200 simulations were conducted in this work. The analysis is divided into two stages. First, we set reference tsunamigenic earthquake scenarios presented in chronological order in the "Reference study" section. For each tsunami source, compiled in Table 2 taken from the previous work and estimate the difference. The purpose of this task is to cover a wide range of information about variability in earthquake source parameters estimated for the same event. Also, exclude outliers (run-up/arrival time) values that cannot be well justified and create a range of possible solutions that constitute the backbone for later evacuation plans. The second stage handles the hypothetical scenarios based on the maximum credible earthquake MCE. At this stage, tsunami hazard is evaluated based on a multiple-scenario approach, considering the possible impact of variability in tsunamigenic earthquake source magnitude and configuration. Incorporating extreme events shall also create a broader perspective of the potential risk by varying its most influential parameters and estimating their relative importance. Practical observations or similar patterns between the different events are investigated and highlighted through both stages. It is worth noting that tsunami intensity measures (e.g., wave height and inland inundation depth) for each point of the AOI and the consequent hazard maps are developed in both stages.

As mentioned previously, a more theoretical yet systematic approach is implemented to handle the potential variability in earthquake parameters and the uncertainty associated with determining their correct values. We found it unfeasible to present all the results of modeling 200 tsunamigenic earthquake scenarios. Therefore, maps and tables show the minimum, maximum, and mean of the percentage of change in the estimated time of arrivals (ETAs) and wave heights and inundation depths. ETA is reported as an instant a positive water surface fluctuation exceeds the assigned threshold of 0.15 m. A clipping boundary for the area of interest is used to determine relevance values.

Additionally, via the histogram classification tool in Geographic Information System (GIS), it is possible to exclude extreme values which do not represent the actual trend. GIS offers a unique set of capabilities for applying location-based analysis to study at hand by using contextual tools to analyze and visualize the data. Throughout this section, all analysis and graphs are produced within the GIS environment using a developed Model Builder environment to speed up the production process.

Table 4 Tsunami intensity measures computed for the 365 scenario at different localities

Parameter	Range value	Governorate							
		Matrouh	Alexandria	El-Beheira	Kafr El-Sheikh	Dakahliya	Damietta	Port Said	North Sinai
Arrival time (min)	Max	71–150	107–113	120–130	127–180	150–180	149–163	165–180	158–180
	Min	57–118	97–109	114–124	50–144	50–146	113–148	118–142	115–150
Wave height (m)	Max	0.9–3.8	1.4–2.8	0.7–1.5	0.4–1.8	0.5–1.0	1.1–1.3	0.07–0.5	0.07–0.8
	Min	0.5–2.0	0.9–1.2	0.5–1.1	0.07–1.0	0.06–0.3	0.2–0.5	0.06–0.07	0.0–0.01
Inundation depth (m)	Max	0.1–1.5	0.3–1.3	0.4–0.8	0.08–0.9	0.09–0.2	0.09–0.3	0.05–0.1	0.09–0.4
	Min	0.06–0.8	0.05–0.6	0.2–0.6	0.0–0.8	0.02–0.1	0.02–0.07	0.0	0.0–0.04

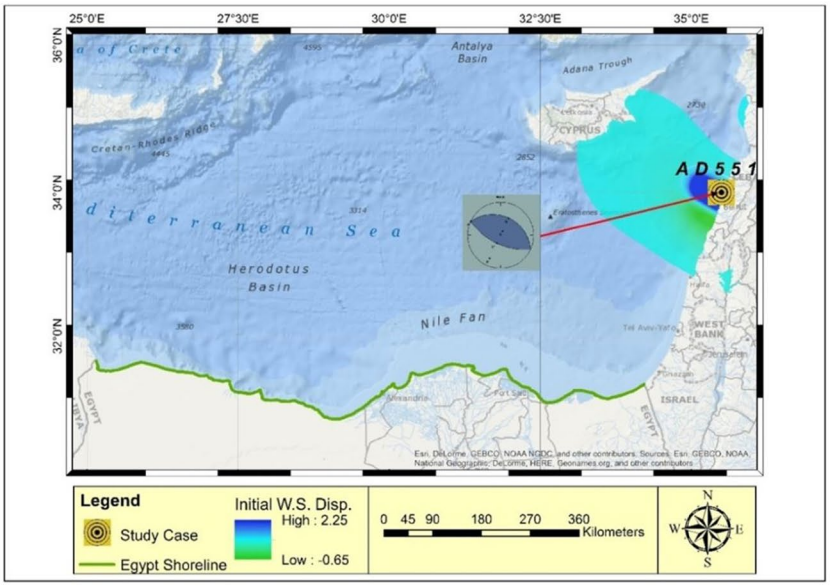

a

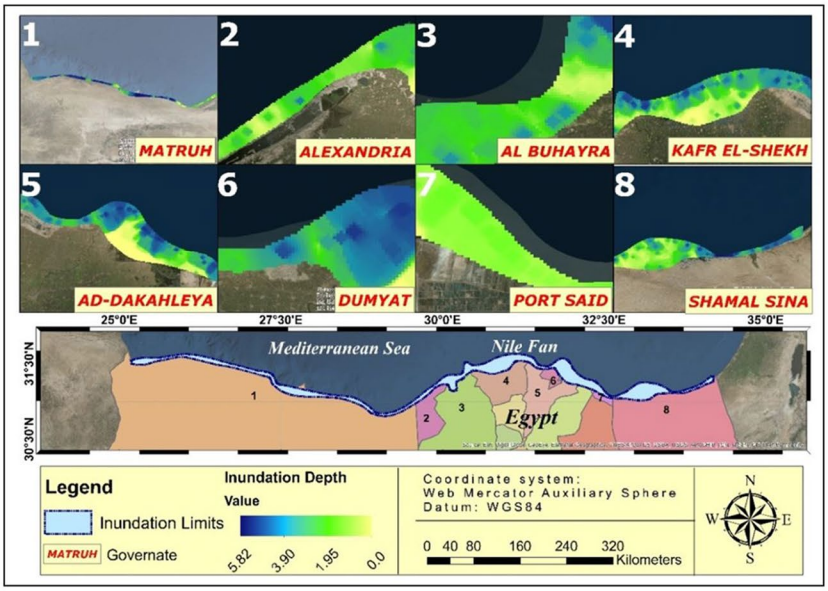

b

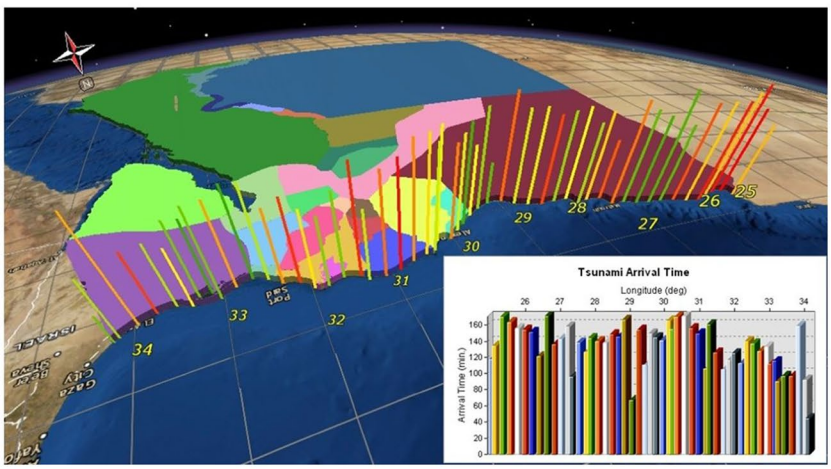

c

Fig. 10 **a** Source location and representative focal mechanism solution of the 551 tsunamigenic earthquake scenario and correspondent initial water surface displacement. **b** Tsunami inundation depth map across the costal of interest computed for the 551 tsunamigenic earthquake. **c** The ETAs distribution along the northern coastline of Egypt defined for the 551 tsunamigenic earthquake scenario. **d** Distribution of maximum tsunami wave height along the northern coastline of Egypt computed for the 551 tsunamigenic earthquake scenario. **e** Top: Mareograms computed at entrance of the Rosetta promontory for the 551 tsunami. Bottom: inundation depth (left)—maximum tsunami wave velocity (right) for the Rosetta promontory. **f** Top: mareograms computed at entrance of the Suez Canal for 551 tsunami scenario. Bottom: inundation depth (left)—wave max. Maximum tsunami wave velocity (right) for the Suez Canal. **g** Comparison between the ETAs and inundation depths obtained in the current results for 551 earthquake tsunami and those of Hamouda (2010b)

Fig. 10 (continued)

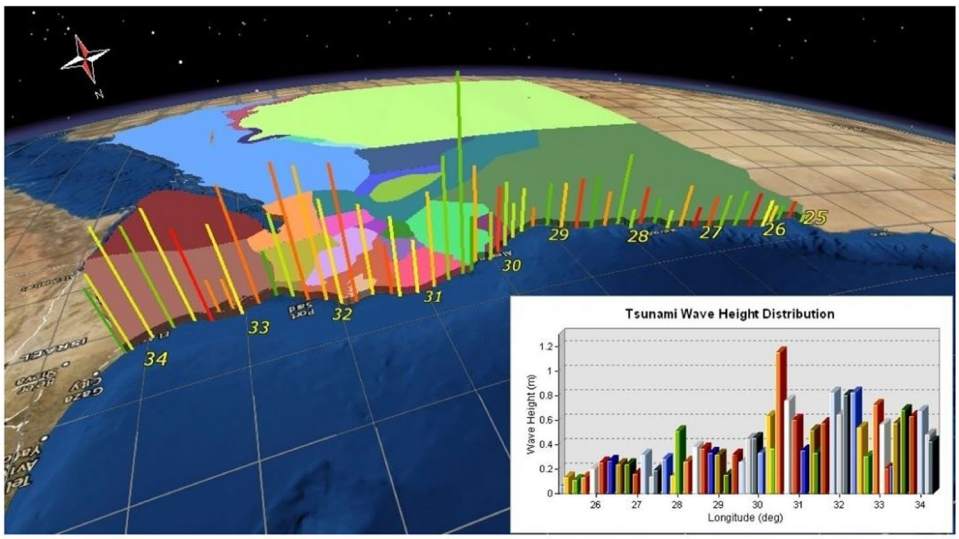

d

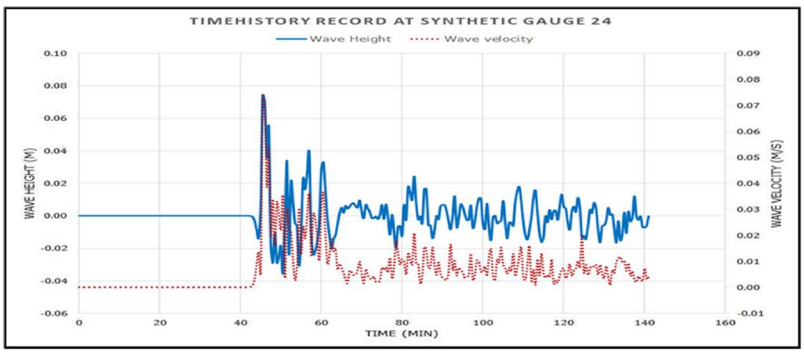

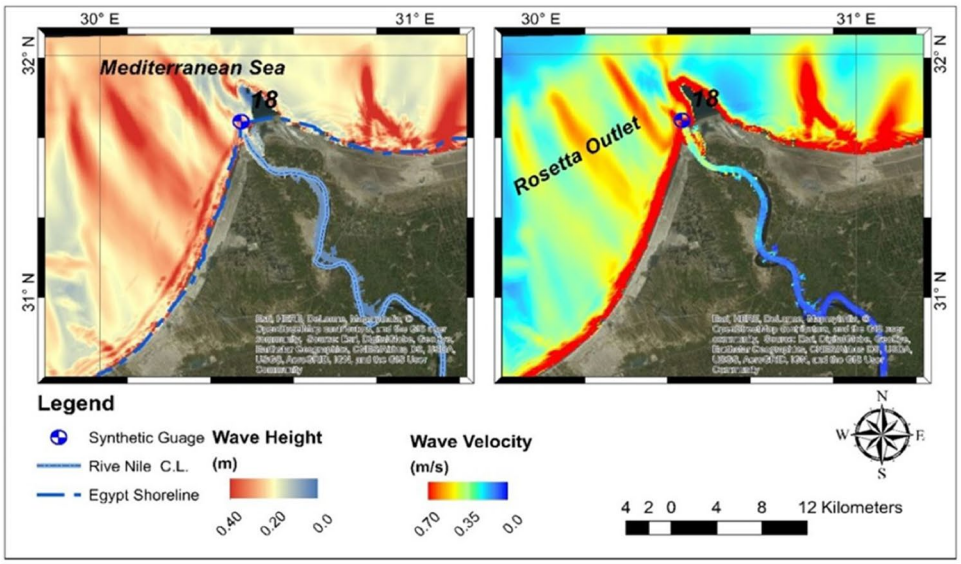

e

Furthermore, due to the statistically limited number of trials, we conducted on each single tsunamigenic earthquake parameter and the fact that the phenomenon under study is both a spatially and temporally varied one, developing significant statistical conclusions from results abstains. Instead, the "General Tendency" is highlighted due to changing any given parameter across all eight test groups. A worst-case scenario for each seismogenic zone is adopted as the basis for comparison across one group.

Fig. 10 (continued)

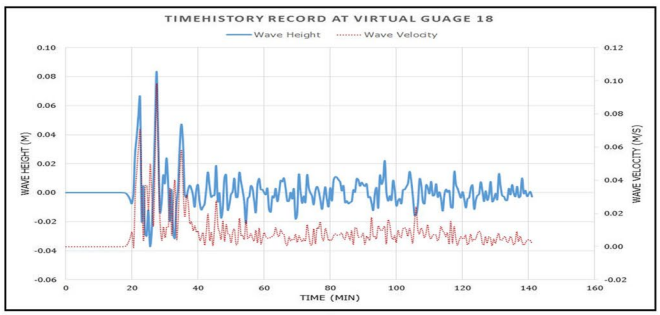

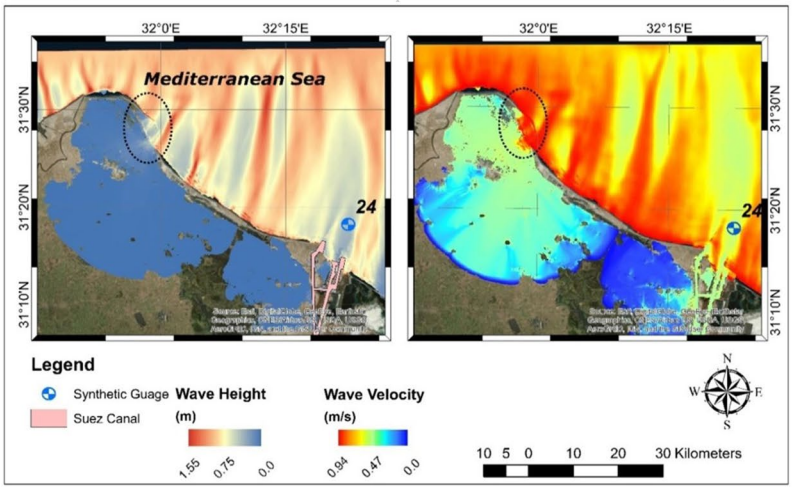

f

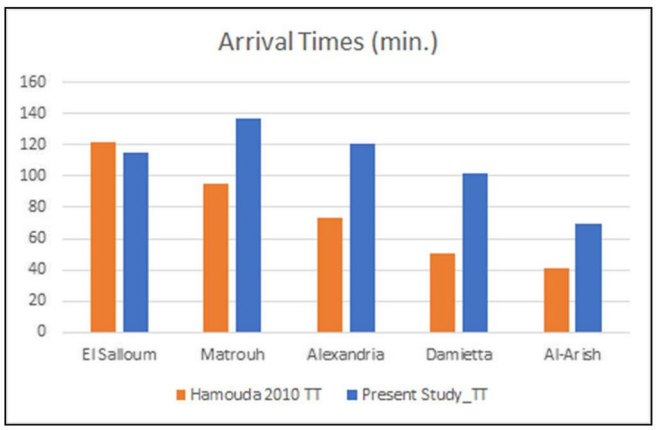

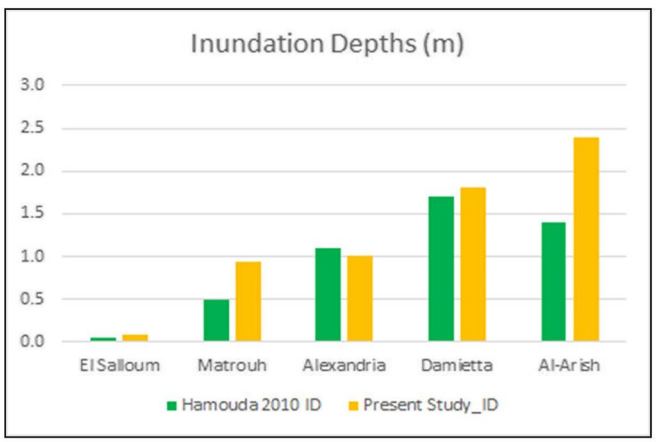

g

Reference study

The 142 CE tsunamigenic earthquake scenario

This event was previously investigated by Mitsoudis et al. (2012), using a probabilistic approach as an alternative to the worst-case scenarios approach for estimating tsunami potential and impact for site-specific studies. Using the same set of tsunamigenic earthquake source parameters in Table 2 and presented in Fig. 8 a based on Okada (1985), the effect that this event may be prone to the coastline of Egypt is defined based on modeling technique NAMI DANCE. See Fig. 8 b all through to Fig. 8 d.

Figure 8 a, b, c, and d indicate the initial water surface displacement, the inundation depth, ETAs, and distribution of heights of tsunami along the coastline, respectively. The maximum estimated value of tsunami wave height is 2.3 m in Kafr El-Sheikh and Damietta governorates Table 3. Also, the min ETAs estimated were 49 and 68 min at Matrouh and Alexandria, respectively.

The computed mareogram at the synthetic gauge no. 18, as shown in Fig. 6, has been extracted to be used as an initial condition (Fig. 8e top). This mareogram is input for detailed tsunami propagation modeling inside the Rosetta promontory. Similarly, the mareogram extracted from synthetic gauge no. 25 (Fig. 8f top) is used to simulate wave propagation into the Suez Canal through its entrance. Simulation time is the same as the original case on the larger domain. The domain boundary is chosen a sufficient distance away from the shoreline to account for all aspects of wave deformation. It is evident from the bottom of Fig. 8 e that just east of the Rosetta promontory, a commercial activity zone could be subjected to an inundation range of 0.6–0.9 m and wave velocity range of 0.5–1.1 m/s due to this scenario. Hence, the COMCOT code is implemented for detailed tsunami propagation in the Rosetta barrage and Suez Canal for all tsunamigenic earthquake scenarios (Fig. 8f).

The 365 CE tsunamigenic earthquake scenarios

This section discusses the potential tsunami hazard of earthquake source that originated in the western segment of the Hellenic trench. The Hellenic arc comprises two segments running parallel to the west section of the trench and mimicking the tsunamigenic source that was very likely responsible for the 365 CE, $M_w = 8.5$ earthquake tsunami. We modeled the 365 tsunami scenarios for the source models listed in Table 2 to assess better the uncertainty related to the rupture process parameters. At this stage, the NAMI DANCE code is adopted to compute the tsunami hazard parameters, as illustrated in Fig. 9 a and f. The initial tsunami condition for this first case is shown in Fig. 9 a. The minimum and maximum water elevation values are extracted and listed in Table 4. A maximum tsunami wave elevation of 3.8 m is estimated at the offshore of Matrouh governorate.

Numerous researchers have intensively investigated the basin-wide impacts of the 365 tsunami tsunamigenic earthquake. Therefore, we modeled tsunamigenic earthquake scenarios developed by Hamouda (2010a and b) and Valle et al. (2014). These researchers used the exact epicenter coordinates for the 365 tsunamigenic earthquake scenarios; however, they adopted different source characteristics with a slight change in earthquake magnitude (Table 2 and Fig. 9a), henceforward referred to as 1st, 2nd, and 3rd source, respectively. It is worth noting that the 365 tsunami was re-investigated under different assumptions in the work of Hamouda (2010a and b). However, no justifications were explicitly given for the modification of source parameters.

A raster calculator toolset in ArcGIS is used to facilitate the extraction of tsunami intensity measures for the three different scenarios for the 365 tsunamigenic earthquake scenarios (i.e., source models) (Fig. 9b, c, d). The results are transformed into raster format and then averaged on a cell by cell basis; wave heights and arrival time distribution of minimum, average, and maximum are extracted in a raster format joining the results obtained from modeling the three scenarios. Also, the minimum and maximum values ETAs and inundation depth along the coastline of each coastal governorate are tabulated in Table 4 to construct an envelope of potential values that may result from variability in source parameters.

To fully understand the variability of the results due to different source models developed by various analysts, we

Table 5 Tsunami intensity measures computed for the 551 scenario at different localities

Parameter	Range value	Governorate							
		Matrouh	Alexandria	El-Beheira	Kafr El-Sheikh	Dakahliya	Damietta	Port Said	North Sinai
Arrival time (min)	Max	167	153	159	166	119	124	142	139
	Min	115	121	120	102	98	102	119	70
Wave height (m)	Max	0.39	0.49	0.63	1	0.73	1	0.74	0.22
	Min	0.06	0.35	0.14	0.39	0.38	0.39	0.19	0.66
Inundation depth (m)	Max	0.94	1.01	0.56	1.54	1.80	1.81	1.62	2.40
	Min	0.06	0.78	0.20	0.17	0.37	0.70	0.46	0.47

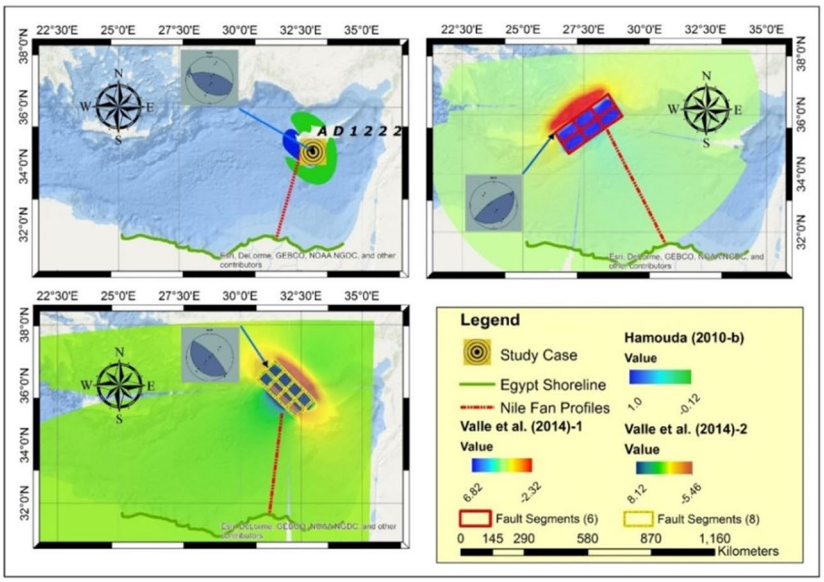

a

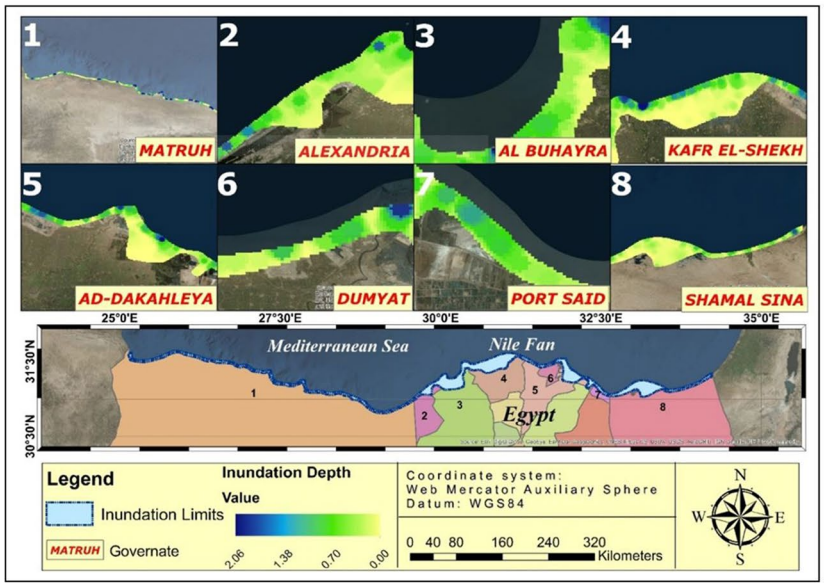

b

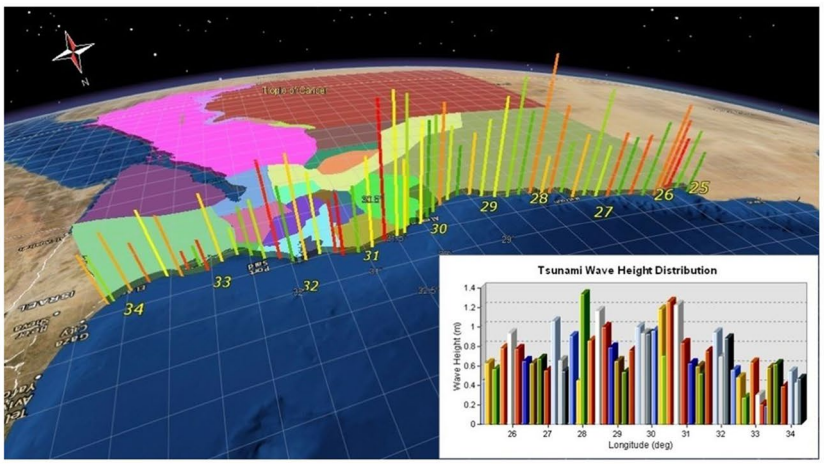

c

Fig. 11 **a** Source location and representative focal mechanism solutions for the 1222 selected tsunamigenic earthquake scenarios and correspondent initial water surface displacement. **b** Maximum tsunami inundation depth map extracted from the 1222 tsunamigenic earthquake scenarios described in Table 2 and panel **a**. **c** The average ETAs distribution along the northern coastline of Egypt defined for the 1222 tsunamigenic earthquake scenarios. **d** Distribution of the maxima tsunami wave height along the northern coastline of Egypt computed for the 1222 tsunamigenic earthquake scenarios. **e** Top: Mareograms computed at entrance of the Rosetta promontory for the 1222 tsunami scenarios. Bottom: inundation depth (left)—maximum tsunami wave velocity (right) for the Rosetta promontory. **f** Top: mareograms computed at entrance of the Suez Canal for the 1222 tsunami scenarios. Bottom: inundation depth (left)-wave max. Maximum tsunami wave velocity (right) for the Suez Canal. **g** Comparisons of minima and maxima of arrival times and inundation depths obtained in this work for the 1222 tsunami with the results of Hamouda (2010b)

Fig. 11 (continued)

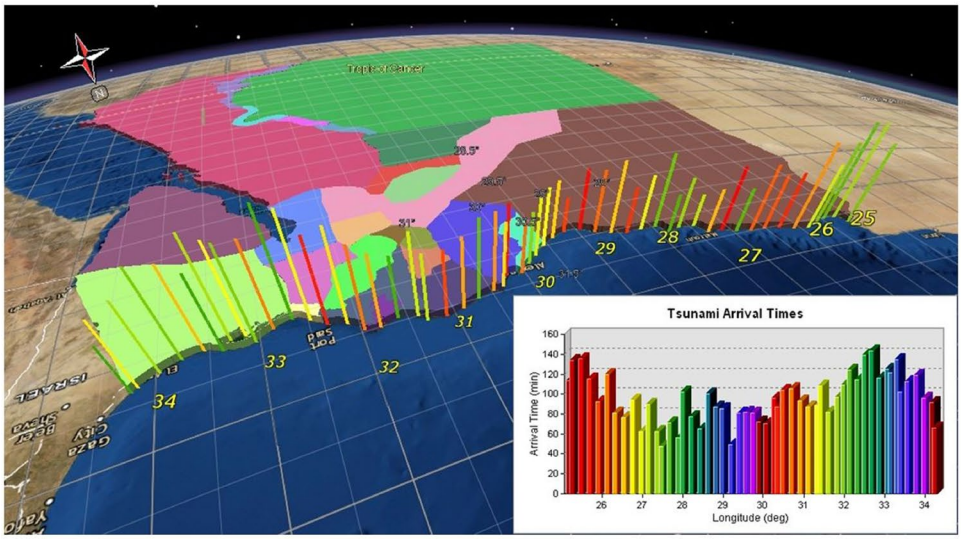

d

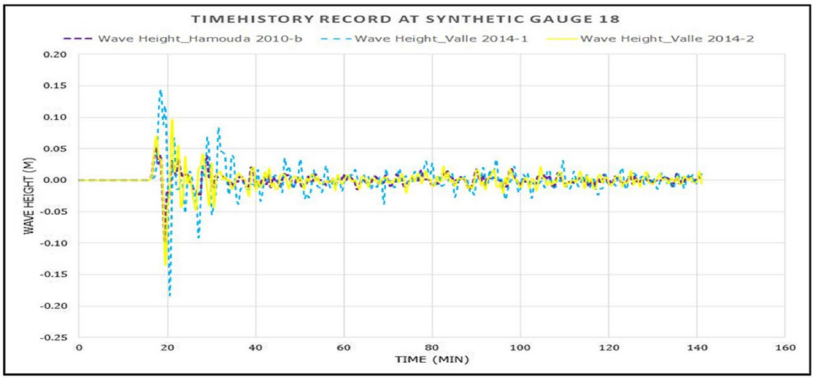

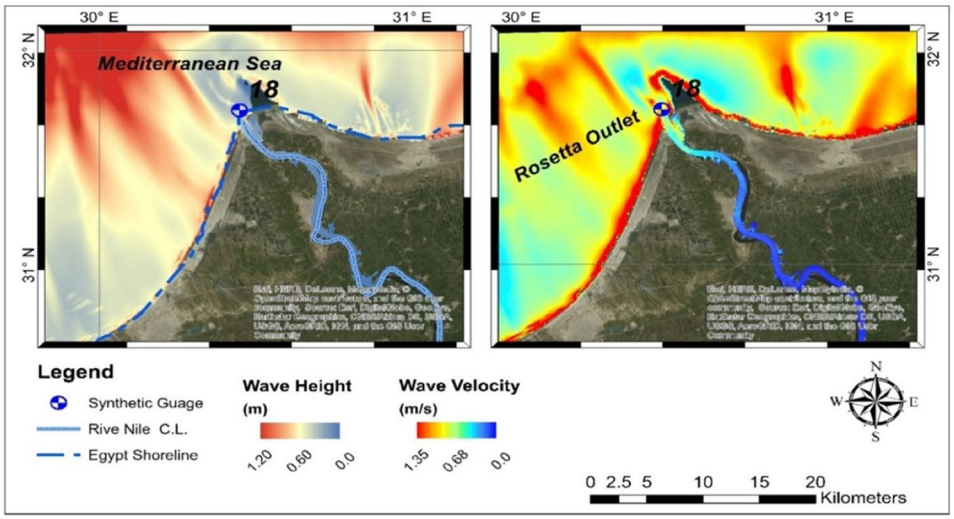

e

must first properly examine the most distinctive features of the source parameters. All three sources share approximately the same strike angle with a maximum difference of 20 degrees (Fig. 9a). Interestingly, the 2nd source, which is characterized by a shallower focal depth compared to the 1st and a smaller source vertical displacement, travels latest, even though it produces more significant initial water surface displacement as can be observed from Fig. 9 a. This again can be accredited to the difference in strike angle. The 2nd source also lags behind the 3rd source even though it has a

Fig. 11 (continued)

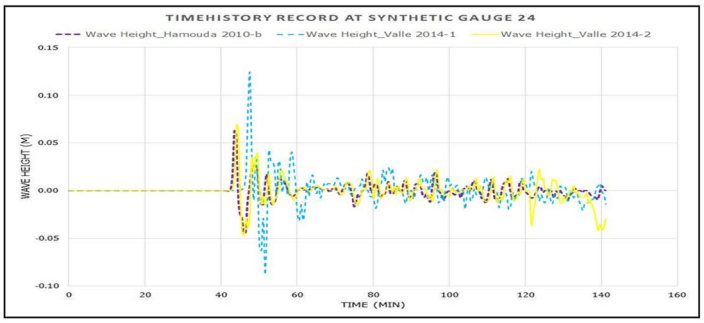

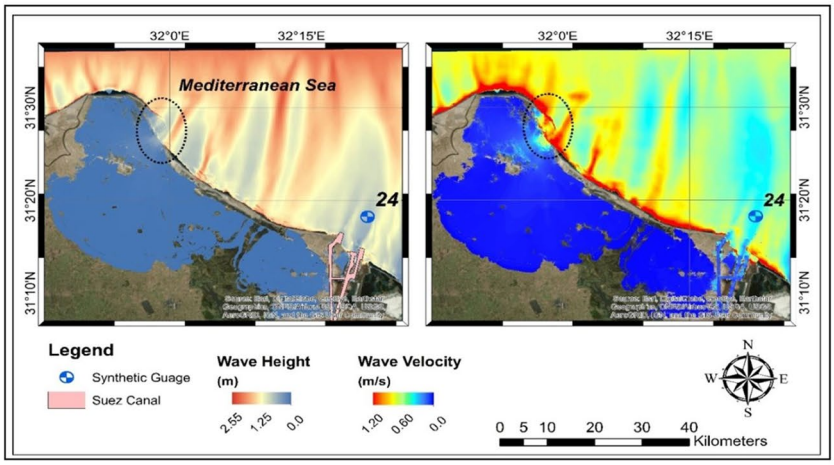

f

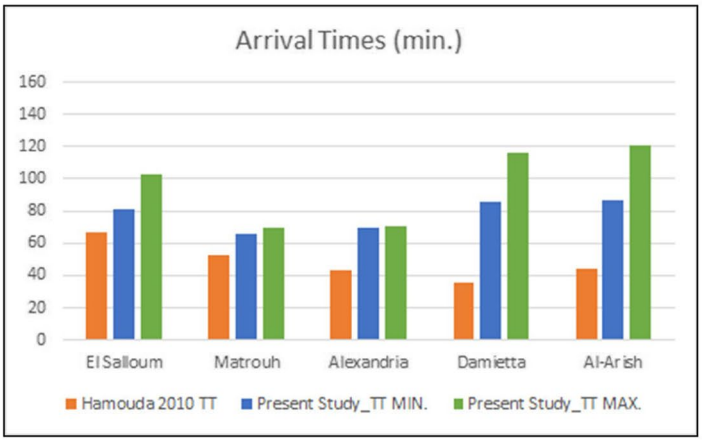

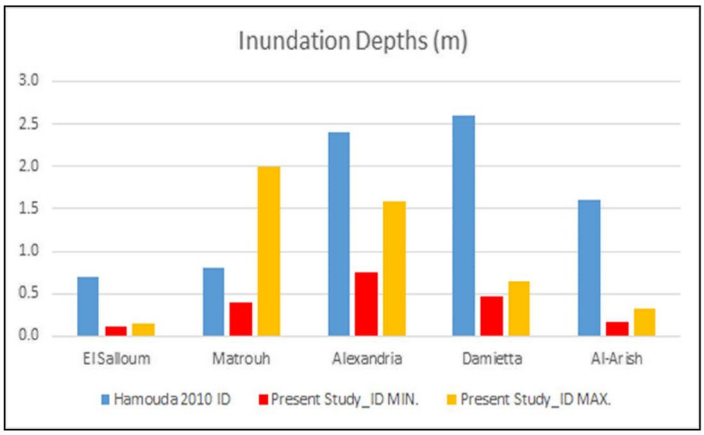

g

smaller strike angle which gives the impression it should travel faster as in the case of the 1st source. We assume another influential factor that may cause this lagging: the vertical source displacement, which is the largest in the 3rd source.

Tsunami wave height, ETAs, and inundation range values along the coastline governorate shown in Fig. 9 c and d are extracted and listed in Table 4. The maximum estimated wave heights of 2.8 and 1.5 m are obtained for the Alexandria and Kafr El-Sheikh governorates, respectively. The inundation area has an almost uniform inundation distribution of approx. 0.0–0.5 m, except for a few regions that have higher inundation values. Tsunami ETAs and wave height distribution are given in Fig. 9 c and d, respectively, showing the maximum wave height closest to the source epicenter. We provide a range of tsunami hazard values from combined three scenarios for 365 tsunami events. Since it could be challenging to compare our findings individually, we can instead indicate the general tendency to agree with their results or diverse noticeably. Also, reaching arrival times and inundation depths as per Hamouda (2010a) to ours in Fig. 9 g top and bottom, respectively.

Similar to 142 tsunamigenic earthquake scenario, mareograms at location of synthetic gauge no. 18 are computed for the three scenarios (top of Fig. 9e), then used to model tsunami propagation inside for detailed tsunami propagation along the Rosetta promontory (bottom of Fig. 9e). Similarly, the mareograms are extracted from synthetic gauge no. 25 (Fig. 9f top) then utilized to simulate wave intrusion into the Suez Canal thought its entrance (bottom of Fig. 9f).

The 551 CE tsunamigenic earthquake scenario

The impacts of the 551 earthquake tsunami on the Egyptian coast have been investigated by Hamouda (2010b) based on simple modeling approach and input data. In the work of Hamouda (2010b), a coarse topo-bathymetry data and a single scenario are adopted. Elias et al. (2007) studied the 551 tsunami to verify its authenticity according to new geophysical data compiled and discussed by Briais et al. (2004). The latest data reveals the existence of seismogenic submarine thrusts offshore of the central part of Lebanon. Figure 10 a illustrates the location, surface water displacement, and focal mechanism of the adopted 551 tsunami earthquake scenario. Tsunami wave propagation pattern from the tsunami source location and ETAs are shown in Fig. 10 c, whereas 50 min is the time required for tsunami waves to travel from the epicenter of the 551 scenario to the Nile Fan.

Figure 10 d indicates a maximum wave height of 1 m offshore Kafr El-Sheikh and Damietta (see also Table 5). The inundated area is reaching a maximum in Buheira, Kafr Elsheikh, Dakahelia, and Damietta; see Fig. 10 b. Figure 10 e indicates that the 551 tsunami scenario does not pose severe threat to the Rosetta promontory than previous scenarios. An inundation depth of 2.4 m, 1.6 m, 1.8 m, and 1.8 m is estimated at offshore locations of North Sinai, Port Said, Damietta, and Kafr El-Sheikh, respectively (Table 5). Also, the wave height and velocity records are extracted. Surely enough, being closer to the source location, the Suez Canal has a more significant threat as waves intrude in Fig. 10 f like all previous scenarios. We can conclude that the 551 scenario may result in a high inundation to the Suez Canal.

The results of the 551 earthquake tsunami modeling obtained by the current work for are different in comparison to those reported by Hamouda (2010b) in terms of propagation patter, wave heights, and ETAs. Seemingly, the results of the current work are more updated in both input data and methodology; hence, the arrival times and wave height obtained in the current study is relatively more significant than those obtained by that primitive work (Fig. 10g). That could be due to the availability of higher resolution of topo-bathymetric data adopted in this work. As for inundation depths, not much difference exists except for the case of Al-Arish and Matrouh cities, both reported with smaller values than our own by approx. 42–47%.

The 1222 CE tsunamigenic earthquake scenario

The 1222 tsunamigenic earthquake is the largest that happened at the Cyprian arc seismogenic source ($M_w \geq 7.5$). Studying the impacts of this tsunami on different areas of

Table 6 Tsunami intensity measures computed for the 1222 scenario at different localities

Parameter	Range value	Governorate							
		Matrouh	Alexandria	El-Beheira	Kafr El-Sheikh	Dakahliya	Damietta	Port Said	North Sinai
Arrival time (min)	Max	65–145	72–83	90–111	68–144	44–149	112–120	143–159	111–159
	Min	53–140	71–79	88–95	59–118	37–122	71–104	116–129	74–140
Wave height (m)	Max	0.76–1.90	1.59–2.45	0.61–1.60	0.70–1.94	0.54–1.79	0.85–1.06	0.28–0.73	0.28–1.02
	Min	0.14–0.59	0.47–0.63	0.21–0.94	0.33–0.97	0.20–0.59	0.33–0.53	0.16–0.47	0.16–0.30
Inundation depth (m)	Max	0.15–1.99	0.35–1.44	0.32–1.15	0.18–1.76	0.12–1.75	0.12–0.69	0.07–0.81	0.07–0.35
	Min	0.11–0.39	0.18–0.51	0.19–0.59	0.10–1.08	0.04–1.08	0.06–0.52	0.05–0.32	0.05–0.16

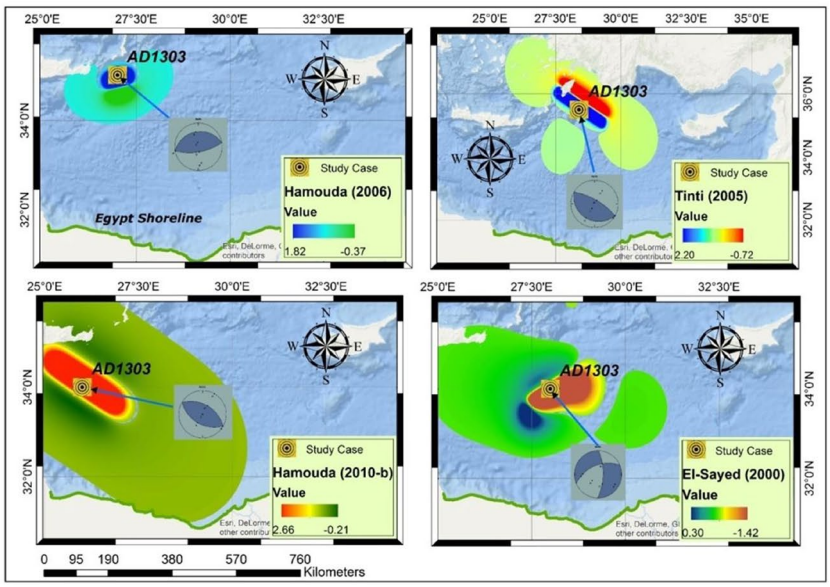

a

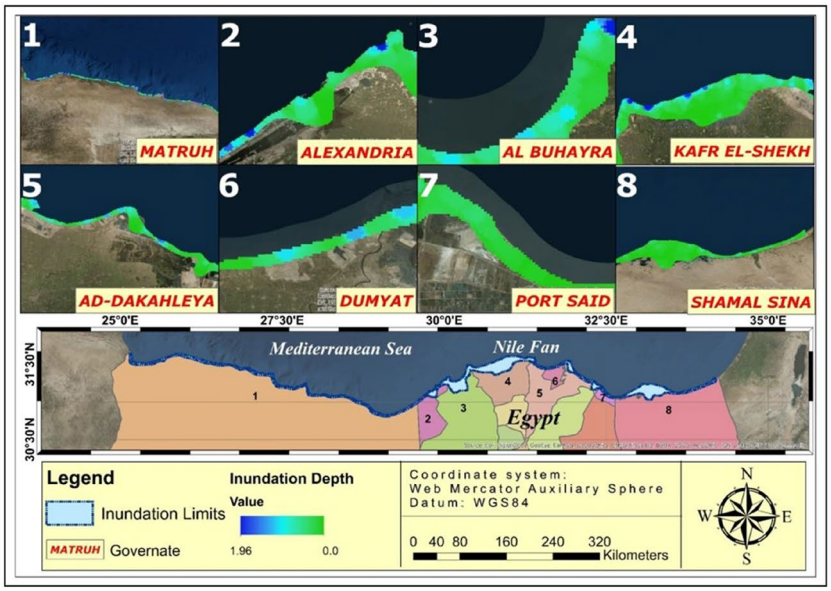

b

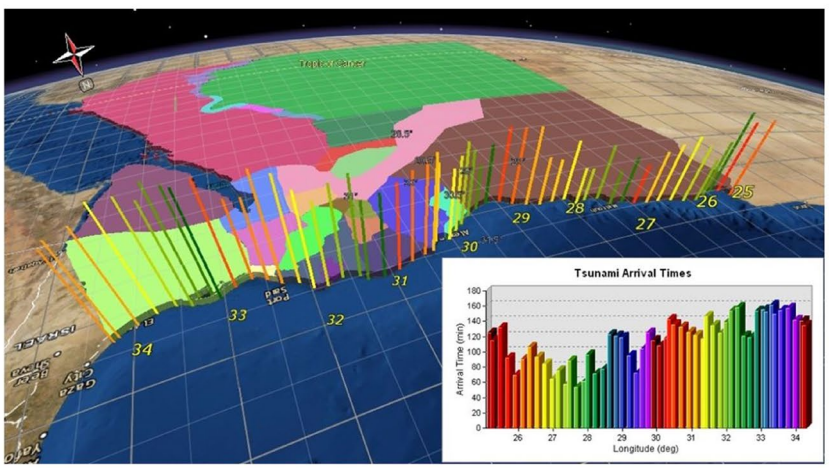

c

Fig. 12 **a** Source location and representative focal mechanism solutions for the 1303 selected tsunamigenic earthquake scenarios and correspondent initial water surface displacement. **b** Maximum tsunami inundation depth map extracted from the 1303 tsunamigenic earthquake scenarios described in Table 2 and panel **a**. **c** The average ETAs distribution along the northern coastline of Egypt defined for the 1303 tsunamigenic earthquake scenarios. **d** Distribution of the maximum tsunami wave height along the northern coastline of Egypt computed for the 1303 tsunamigenic earthquake scenarios. **e** Top: mareograms computed at entrance of the Rosetta promontory for the 1303 tsunami. Bottom: inundation depth (left)—maximum tsunami wave velocity (right) for the Rosetta promontory. **f** Top: mareograms computed at entrance of the Suez Canal for the 1303 tsunami. Bottom: inundation depth (left)—maximum tsunami wave velocity (right) for the Suez Canal. **g** Comparisons of minima and maxima of arrival times and inundation depths obtained in this work for the 1303 tsunami with the results of Hamouda (2010b)

Fig. 12 (continued)

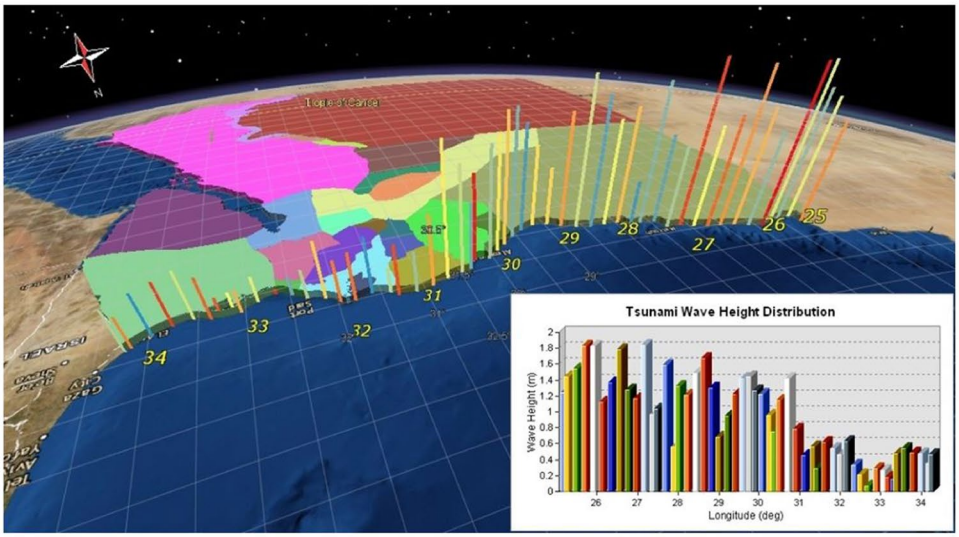

d

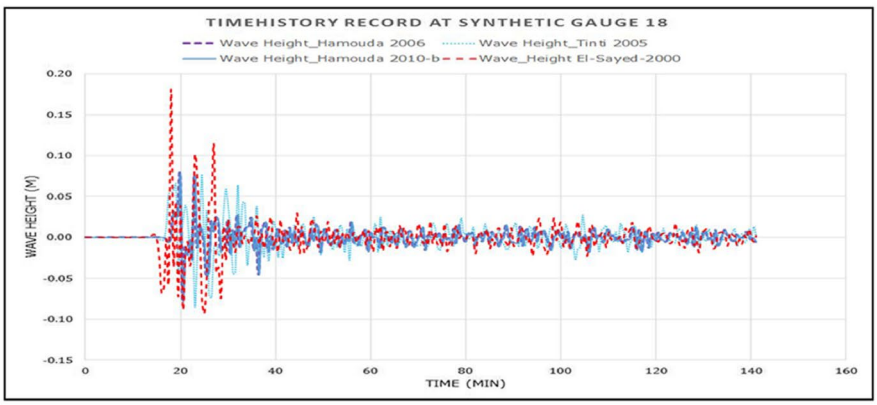

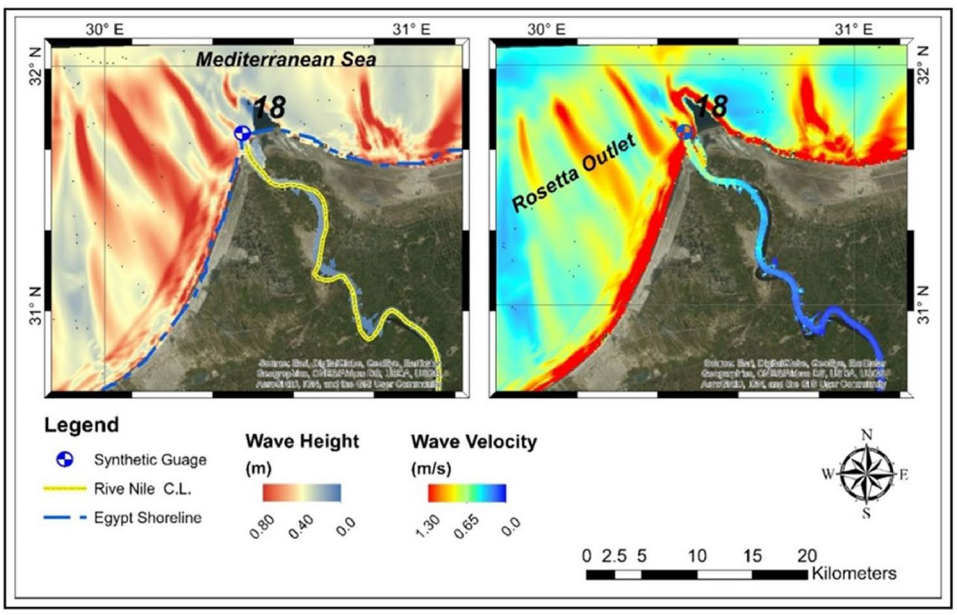

e

Fig. 12 (continued)

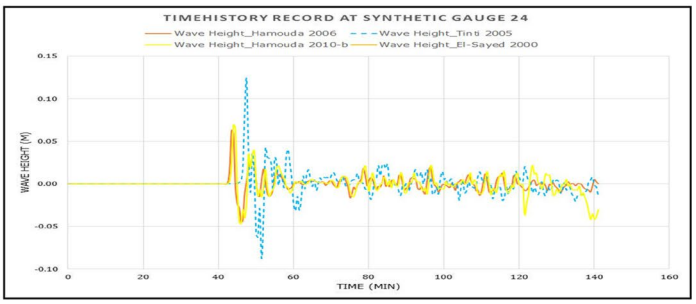

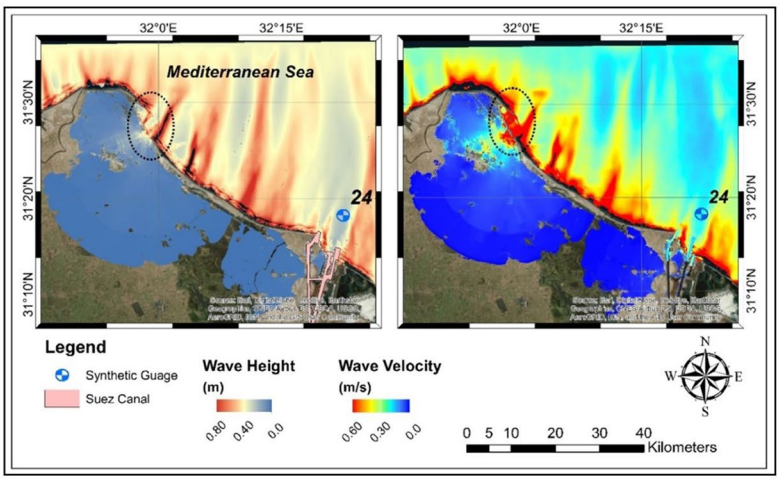

f

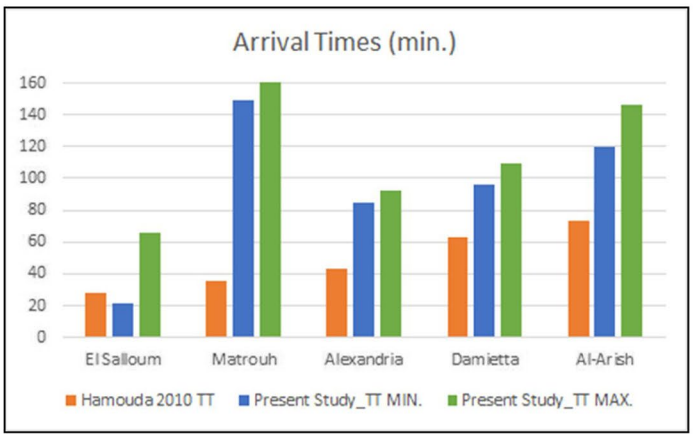

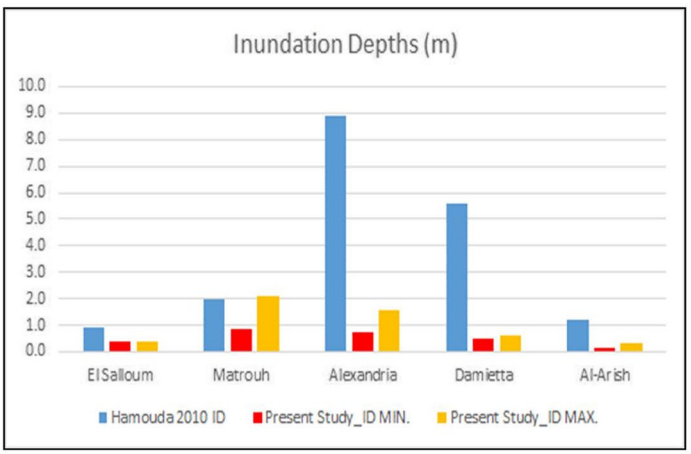

g

interest has attracted due attention of many researchers (e.g., Hamouda 2010b; Valle et al. 2014). While Hamouda (2010b) has utilized a single scenario to characterize the tsunami hazard related to this tsunamigenic source, Valle et al. (2014) have adopted two different scenarios in their simulations of different fault configurations to consider possible source variability (Fig. 11a). These three different scenarios are referred to as 1st, 2nd, and 3rd scenario, which represent Hamouda (2010b), two tsunami scenarios of Valle et al. (2014), respectively (Fig. 11a).

The ETAs and inundation maps (Fig. 11b, c, d) show different propagation patterns developed for each scenario and the impact on the arrival time of tsunami waves. The maximum wave elevation, inundation depth, and ETAs are obtained. A summary of main tsunami hazard measures for the 1222 scenarios described in Table 2 is listed in Table 6. The upper bound wave height map obtained from the three tsunami scenarios shows a maximum of 0.7–2.5 m across the Nile Delta's coastal area (Table 6). The maximum positive wave amplitudes (water elevations) at every grid point computed during simulation duration for the 1222 scenarios are presented in Fig. 11 d. Also, it shows that extreme impacts could occur at the eastern side of the Rosetta promontory until Arish city. The first tsunami wave arrives at the Dakahliya coast after 44 min from earthquake occurrence with negative amplitude as indicated by Fig. 11 c.

The detailed analysis for the Rosetta promontory and the Suez Canal exhibits a characteristic behavior of tsunami interaction within these two sites (Fig. 11e, f), whereas high velocities along the shoreline and large inundated regions are deduced to the west of the Suez Canal correspond to Manzala Lake, the largest of the northern coastal lagoons of Egypt which is an indispensable source of fish for human consumption. Also, when comparing values extracted from Hamouda (2010b) results with the results obtained in this work, we notice a consistent difference in arrival times and inundation depths. The average increase in our results is 22–64% for arrival times and an average decrease of 51–84% in inundation depth across the whole coast of interest except for the city of Matrouh.

The 1303 CE tsunamigenic earthquake scenarios

The 1303 earthquake tsunami of $M_w \sim 8.0$ originated offshore Crete Island and is the largest known event in the historical catalogue. Table 2 lists the fault parameters adopted by different existing studies to model the potential tsunami threats from the East Hellenic Arc tsunamigenic earthquake source. We modeled four different fault rupture models (scenarios) for the 1303 tsunami which are listed in Table 2. These models were developed by different authors to assess the possible hazard of EHA (Fig. 12a). The results of the modeled multi-scenario can be used to produce the map of mean or other percentiles based on their choices and amount of conversion as shown in Fig. 12 b, c, and d. Indeed, by examining the propagation pattern for each scenario, we can observe various propagation patterns associated with different strike directions and subsequent incident wave angles.

This tsunami event and its impacts were primarily investigated by many researchers across the EMB for different target locations (Hamouda 2006, 2010b; Tinti et al. 2005; El-Sayed et al. 2000). Throughout this section, four scenarios developed for the 1303 tsunami are modeled and then combined statistically to obtain the extreme and average tsunami hazard parameters. These scenarios are named the 1st, 2nd, 3rd, and 4th, respectively. These scenarios have different epicenter locations, as indicated in Table 2 and Fig. 12 a, which means different propagation patterns and impacts (Fig. 12 b, c, d). We follow the same strategy adopted in the previous tsunamigenic earthquakes for extracting tsunami hazard parameters, i.e., inundation depths, wave height, and arrival times, by combining results from all four scenarios. Tsunami intensity measures computed for the 1303 scenario at different localities are listed in Table 7. The shortest ETA is estimated for Alexandria 56 min and a maximum wave elevation of 2.5 m.

Figure 12 e and f indicate the computed mareograms and detailed analysis of tsunami wave propagation inside the Rosetta promontory and the Suez Canal, respectively. Inundation depths and wave velocities around the Rosetta promontory and the Suez Canal are well within the average of all values observed so far. Inspecting Fig. 12 a, we can

Table 7 Tsunami intensity measures computed for the 1303 scenario at different localities

Parameter	Range value	Governorate							
		Matrouh	Alexandria	El-Beheira	Kafr El-Sheikh	Dakahliya	Damietta	Port Said	North Sinai
Arrival time (min)	Max	66–175	56–75	92–141	92–172	120–161	109–138	160–174	146–180
	Min	21–149	30–69	85–128	85–163	114–149	96–124	149–170	120–169
Wave height (m)	Max	0.44–2.54	1.50–2.54	0.83–1.50	0.46–1.50	0.48–0.85	0.50–0.85	0.20–0.48	0.17–0.69
	Min	0.43–1.53	1.09–1.35	0.51–1.12	0.40–1.11	0.40–0.58	0.40–0.57	0.13–0.40	0.13–0.37
Inundation depth (m)	Max	0.39–2.07	0.88–1.58	0.37–0.74	0.30–0.80	0.25–0.63	0.54–0.64	0.04–0.28	0.04–0.33
	Min	0.36–0.86	0.51–0.75	0.16–0.52	0.11–0.61	0.13–0.61	0.19–0.47	0.0–0.11	0.0–0.17

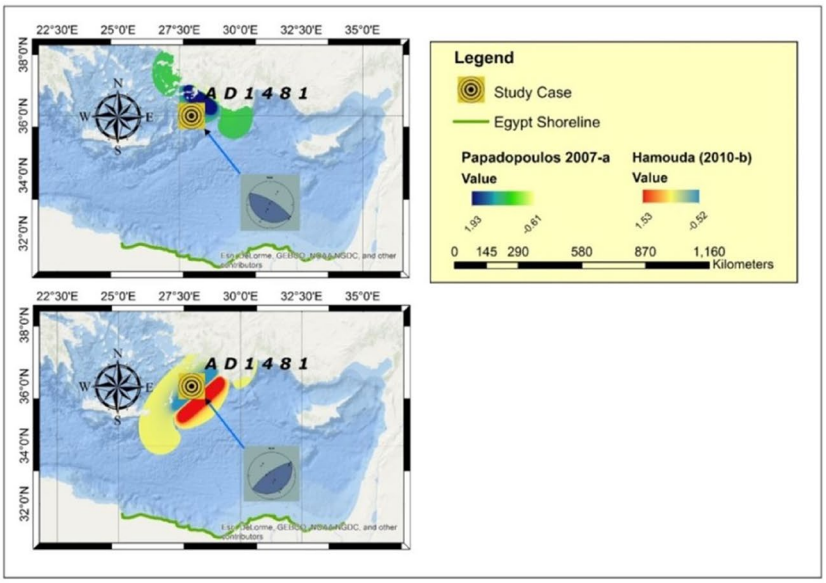

a

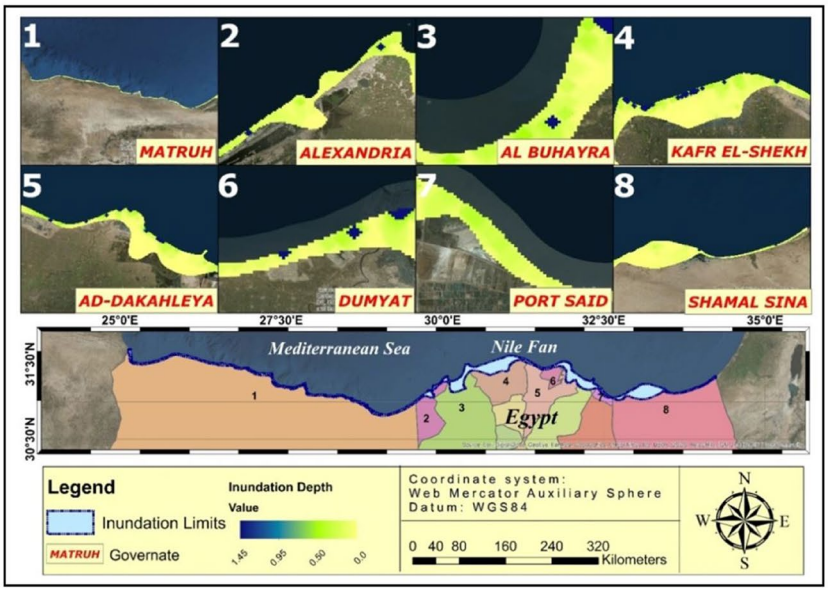

b

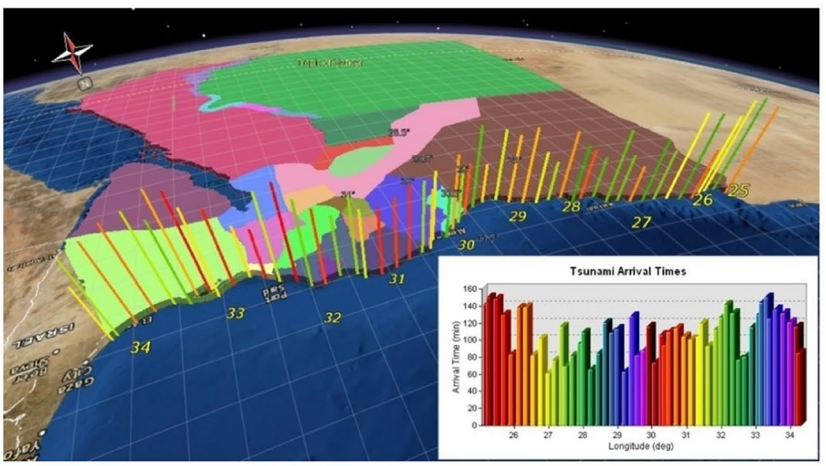

c

Fig. 13 **a** Source location and representative focal mechanism solutions for the 1481 selected tsunamigenic earthquake scenarios and correspondent initial water surface displacement. **b** Average tsunami inundation depth map extracted from the 1303 tsunamigenic earthquake scenarios described in Table 2 and panel **a**. **c** The average ETAs distribution along the northern coastline of Egypt defined for the 1481 tsunamigenic earthquake scenarios. **d** Distribution of average of the maxima tsunami wave height along the northern coastline of Egypt computed for the 1481 tsunamigenic earthquake scenarios. **e** Top: mareograms computed at entrance of the Rosetta promontory for the 1481 tsunami. Bottom: inundation depth (left)—maximum tsunami wave velocity (right) for the Rosetta promontory. **f** Top: mareograms computed atentrance ofthe SuezCanal for the 1481 tsunami. Bottom: inundation depth (left)—maximum tsunami wave velocity (right) for the Suez Canal. **g** Top: mareograms computed at entrance of the Suez Canal for the 1481 tsunami. Bottom: inundation depth (Left); maximum wave velocity (Right) for the Suez Canal

Fig. 13 (continued)

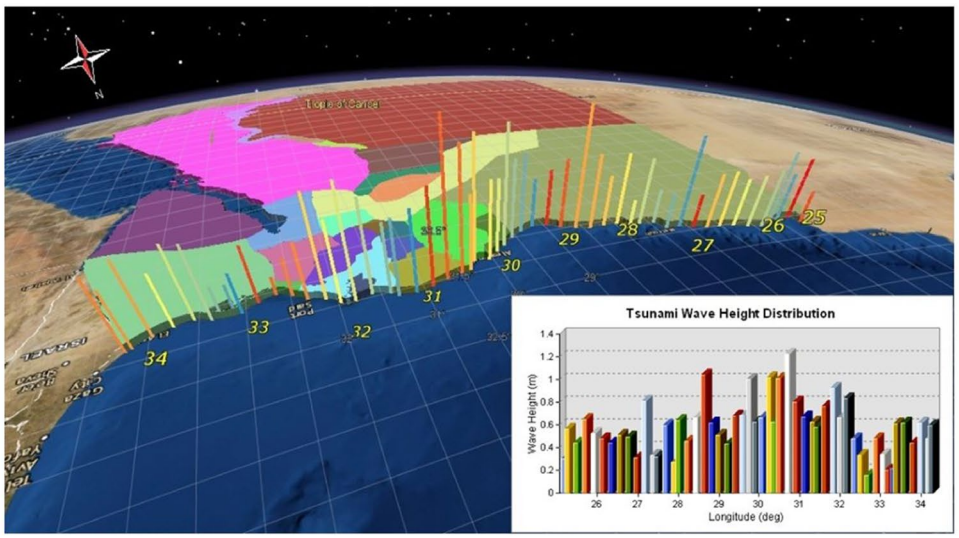

d

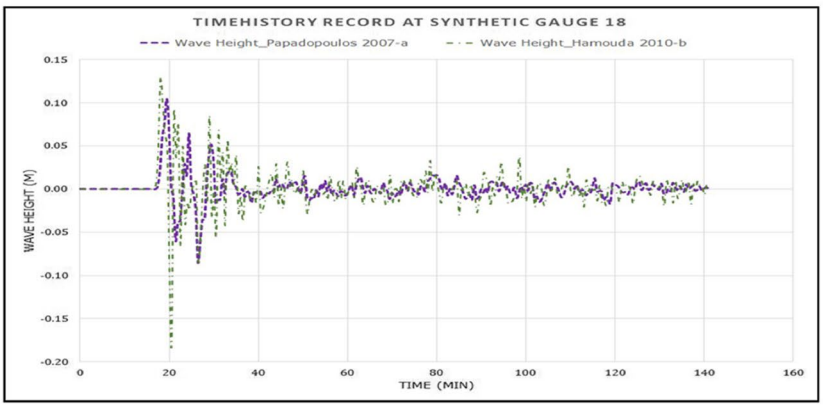

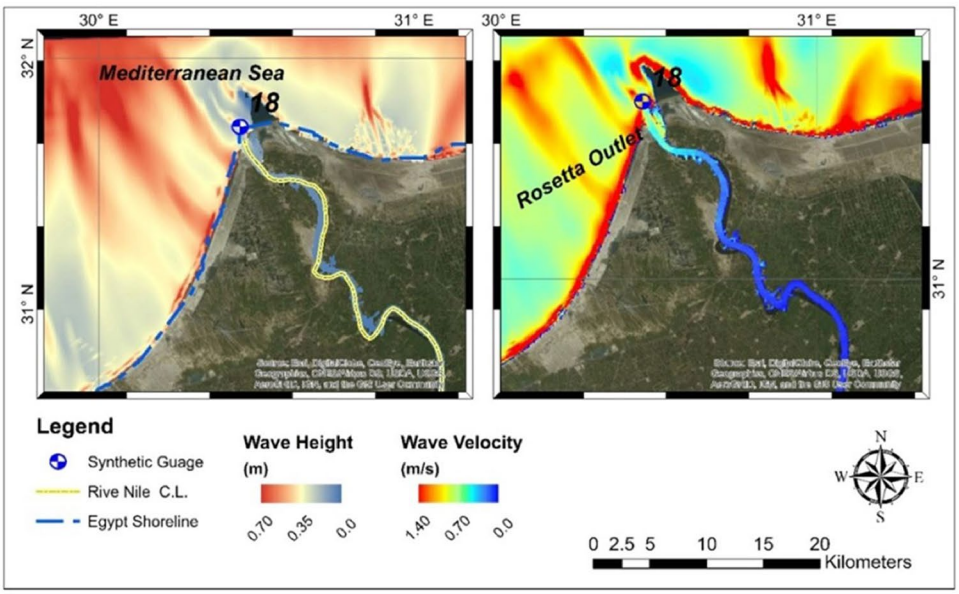

e

Fig. 13 (continued)

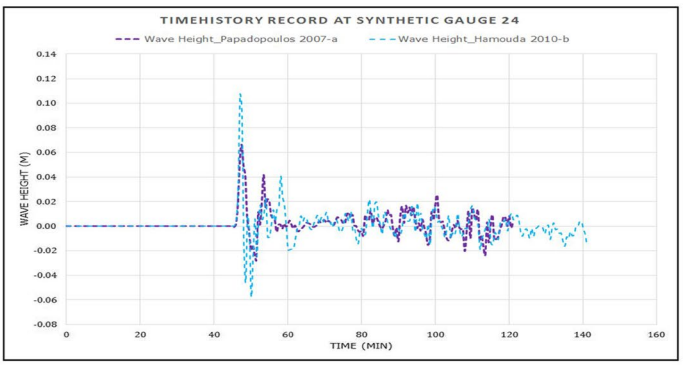

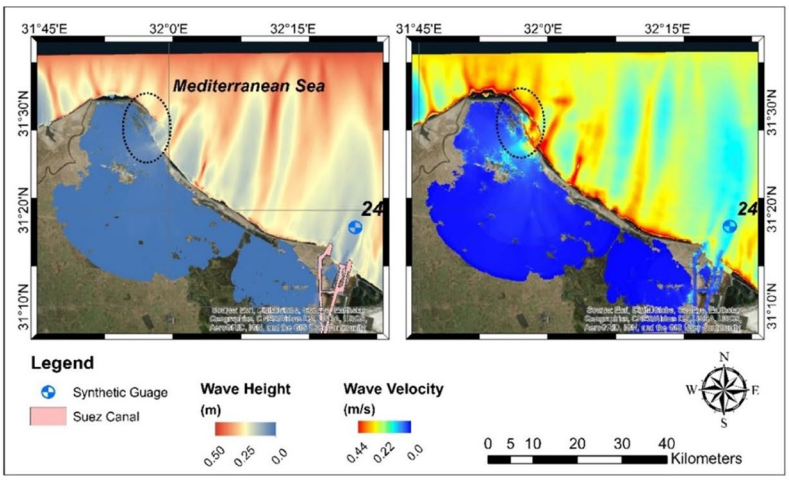

f

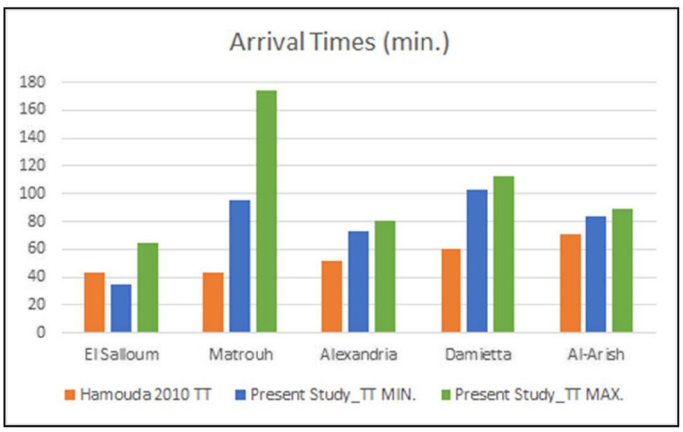

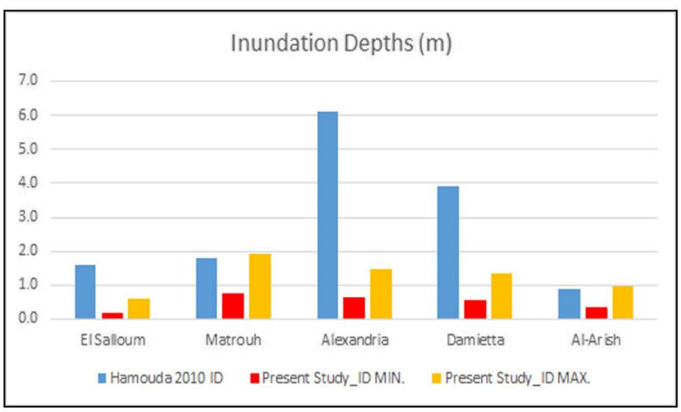

g

Table 8 Tsunami intensity measures computed for the 1481 scenario at different localities

Parameter	Range value	Governorate							
		Matrouh	Alexandria	El-Beheira	Kafr El-Sheikh	Dakahliya	Damietta	Port Said	North Sinai
Arrival time (min)	Max	65–174	81–98	104–125	110–148	118–150	112–129	147–160	89–160
	Min	35–95	73–86	91–96	91–143	67–147	103–120	142–150	84–150
Wave height (m)	Max	0.28–1.10	0.92–1.10	0.68–1.15	0.73–1.94	0.87–1.46	1.27–1.51	0.32–1.22	0.31–1.14
	Min	0.21–0.69	0.42–0.69	0.36–0.56	0.38–0.65	0.25–0.57	0.37–0.54	0.13–0.32	0.13–0.38
Inundation depth (m)	Max	0.60–1.91	1.16–1.46	0.13–1.20	0.27–1.33	0.60–1.80	0.36–1.33	0.05–0.71	0.05–0.96
	Min	0.17–0.75	0.42–0.62	0.16–0.45	0.20–0.68	0.13–0.49	0.23–0.56	0.0–0.24	0.0–0.33

Table 9 Adopted classification of values based on ratio between reference case and hypothetical scenarios Δ (%)

Classification	Arrival times Δ (%)	Wave heights Δ (%)	Inundation depths Δ (%)
MINIMAL	− 12 <	< − 10	< 30
MODERATE	− 38–12.1	− 10.1–70	30.1–60
SIGNIFICANT	− 64–38.1	70.1–150	60.1–90
SEVERE	< − 64.1	150.1 <	90.1 <

say that there is little difference in arrival times compared to Hamouda (2010b). In contrast, the differences even more in inundation depths, especially for Alexandria and Damietta. The comparison of the results of extreme values for wave height and ETA obtained by the current work and those of Hamouda (2010b) indicate that the current study provides a much smaller estimate at the selected sites (see Fig. 12 g).

The 1481 CE tsunamigenic earthquake scenarios

Although 1481 tsunami has a reliability rank of 4, i.e., definite tsunami by NGDC/WDS, few tsunami hazard studies were carried to investigate its impacts on the Egyptian coastline (i.e., Papadopoulos et al. 2007 and Hamouda 2010b). The event epicenter location lies approx. 630 km away from the nearest Egyptian shoreline, which is one reason why it takes relatively more time to reach the continental shelf (90–100 min), whereas previous scenarios being investigated in this work occurred at the Hellenic Arc seismogenic source have shorter ETAs (Fig. 13 a, b, c). Two tsunami source models for the 1481 tsunami are addressed in this work. The epicentral location and source parameters for these models are listed in Table 2, and presented in Fig. 13 a. Also, a regionalized inundation map and zoomed ones for selected localities along the coastline are shown in Fig. 13 b. The distribution of the average of the maxima tsunami

Table 10 Summary of hypothetical scenarios comparison to reference case of the 142 CE tsunami

Test parameter		Δ from ref. case	Δ in travel times (%)			Δ in wave heights (%)			Δ in inundation depths (%)		
			MIN	MAX	MEAN	MIN	MAX	MEAN	MIN	MAX	MEAN
Reference case	Value	NONE	38.83	176.7	106.0	0.0	0.90	0.12	0.0	4.2	0.87
Rake (o)	70	− 40	− 35.4	28.6	− 3.3	− 23.9	20.3	− 3.6	− 1.3	1.0	− 0.2
	90	− 20	− 38.8	26.3	− 2.9	− 23.2	21.2	− 1.8	− 3	2.3	− 0.4
Strike (o)	155	+ 40	− 32.4	108.8	19.5	− 62.5	61.0	− 12.2	− 6.3	5.4	− 0.3
	270	+ 155	− 47.4	17.8	− 5.4	− 42	87.8	21.5	− 1.2	4.7	0.7
Vert. Disp.(m)	2.55	0.34	− 24.1	21.7	− 0.8	− 30.3	53.3	11.1	− 1.8	2.6	− 0.1
Focal Depth (km)	20	+ 7	− 22.8	19.9	− 1.2	− 49	30.4	− 9.7	− 3.9	1.5	− 0.7
	25	+ 12	− 24.4	20.5	− 1.4	− 55	31.0	− 14.7	− 6.1	2.3	− 0.6
Mag	7	− 0.7	− 37.7	40.8	3.8	− 86	− 62.0	− 76.3	− 12	0.0	− 1.9
	8.4	+ 0.7	− 71.9	94.2	− 8.1	7.6	717.8	281.7	0.4	25.8	6.7
	8.9	+ 1.2	− 70.9	74.1	− 14.9	118.9	3188.1	1346.4	1.1	71.8	18.4
SLR 45 (cm)	37.50	+ 37.5	− 39.3	35.9	− 2.1	− 31.9	55.7	3.3	− 4.3	31.6	7.7
	90.60	+ 90.6	− 53.6	49.2	− 3.1	− 28.1	43.8	0.7	− 20.4	115.1	6.2
SLR 85 (cm)	55.60	+ 55.6	− 46.4	41.6	− 2.2	− 43.2	67.7	1.5	− 12.5	73.8	4.3
	112.80	+ 112.8	− 54	47.9	− 3.5	− 36.5	91.8	13.8	− 32.2	140.9	11.5

wave height along the northern coastline of Egypt computed for the 1481 tsunamigenic earthquake scenarios is shown in Fig. 13 d. The variability tsunami maximum wave height ranges between 0.2 and 1.2 m (Table 8). Tsunami intensity measures are calculated for the 1481 scenario at different coastal governorates. The shortest ETAs have been estimated for Matrouh and Alexandria governorates 65 and 81 min, respectively.

Inundation depth and wave velocity maps for the Rosetta promontory and the Suez Canal are demonstrated in Fig. 13 e and f. The mareograms are shown at the top of Fig. 13 e, and f are adopted to calculate maximum velocity and wave height impacts for the two strategic sites, as shown at the bottom these figures.

Moreover, the comparison between the results of this work with Hamouda (2010b) is shown in Fig. 13 g. The ETAs computed by Hamouda (2010b) at some selected sites seem smaller relative to those calculated in this study, which means they travel faster than values from his work. However, the maximum wave heights computed by Hamouda (2010b) are higher than the values obtained in this work for all the selected sites as shown in Fig. 13 g.

Hypothetical scenarios

As mentioned previously, a systematic approach is implemented to handle the possible variability of earthquake parameters and embrace potential uncertainty. Also, the SRL and the Nile Delta subsidence models are considered. Therefore, we decide to illustrate the degree of change in the tsunami hazard intensity parameters (Table 9). Our rationale for color coding is explained in this fashion: only minimum ETAs gets color coded, as they entitle faster arrival of a tsunami wave, hence more risk due to shorter evacuation less time. On the contrary, maximum values for wave heights and inundation depths were color-coded as they induce more danger when they get higher. We found it more feasible to summarize the obtained results in terms of tables exhibiting the minimum, maximum, and mean of the change in arrival time's percentage, wave heights, and inundation depths relative to reference cases shown in Tables 10, 11, and 12. A clipping boundary for the area of interest is used to determine relevance values. Additionally, via the histogram classification tool in ArcGIS, it is possible to exclude extreme values which do not represent the actual trend.

Following the results extracted from the hypothetical scenarios and the colored classification in the previous section, an additional explanation of their relative effect on tsunami wave characteristics will be further discussed.

Decreasing rake angle from strike-slip to simple dip-slip mechanism reduces travel time. The degree changes depending on the case being minimal/moderate in most cases, e.g., a 35–40% reduction in case of 142 CE tsunami. On the contrary, wave heights and inundation depth are reduced by 20% in case of 142 CE and 2.3% in inundation depth (Tables 10–12 and Figs. 14, 15, 16a, b, c).

Strike angle is designing the tsunami wave propagation (closely correlated with incident wave angle in the deep waters). In this regard, in case 142, as the propagation front is directed to the Egyptian coast with each increase of strike angle, we can observe the following: a moderate to significant decrease/increase in travel times/wave heights, respectively. The effect on inundation depth is less significant, but the value rises nevertheless. The same observation can be

Table 11 Summary of hypothetical scenarios comparison to reference case of the 365 CE tsunami

Test parameter		Δ from ref. case	Δ in travel times (%)			Δ in wave heights (%)			Δ in inundation depths (%)		
			MIN	MAX	MEAN	MIN	MAX	MEAN	MIN	MAX	MEAN
Default case	Value	NONE	65.2	180.0	133.8	0.0	1.8	0.3	0.0	5.6	0.8
Rake (o)	70	−29	−39.3	25.8	−13.7	−33.1	44.5	−1.5	−6.9	2.8	−1.2
	110	+11	−1.0	2.2	0.2	−27.8	11.3	−4.5	−1.6	1.5	−0.1
Strike (o)	115	−200	−46.5	73.4	0.2	−99.3	100.4	−17.8	−8.3	4.6	−1.8
	150	−165	−67.8	57.2	1.8	−59.3	143.7	3.1	−8.1	7.0	−0.3
Vert. Disp.(m)	6.63	+0.86	−1.2	0.7	−0.2	2.6	25.7	14.1	0.0	6.0	1.4
Focal Depth (km)	10.3	−3.7	−0.6	0.5	0.1	−15.9	9.5	−3.3	−1.0	0.8	−0.1
	20	+5.0	−0.8	1.1	0.1	−6.7	14.5	1.8	−1.0	1.0	0.0
Mag	8	−0.5	−25.0	35.3	1.2	−98.8	−56.8	−78.5	−14.5	0.0	−4.4
	9	+0.5	−57.0	102.9	5.6	−17.3	644.5	210.4	−1.4	66.8	11.4
SLR 45 (cm)	37.50	+37.5	−2.8	1.9	−0.5	−18.3	48.2	4.9	−7.2	30.0	2.0
	90.60	+90.6	−5.2	2.5	−0.8	−46.0	90.7	24.9	2.6	83.9	16.8
SLR 85 (cm)	55.60	+55.6	−4.3	3.2	−0.6	−11.0	50.6	4.6	−2.9	55.3	10.3
	112.80	+112.8	−8.1	4.6	−1.2	−22.5	62.6	7.1	−0.5	86.9	17.4

Table 12 Summary of hypothetical scenarios comparison to reference case of the 1481 CE tsunami

Test parameter		Δ from ref. case	Δ in travel times (%)			Δ in wave heights (%)			Δ in inundation depths (%)		
			MIN	MAX	MEAN	MIN	MAX	MEAN	MIN	MAX	MEAN
Default case	Value	NONE	50.5	180.0	143.2	0.0	0.4	0.1	0	6.7	0.4
Rake (o)	70	−40	−16.1	15.4	−0.4	−24.3	32.1	−1.8	−0.3	0.3	0.0
	90	−20	−0.7	1.0	0.2	−12.8	22.0	2.9	−0.1	0.2	0.0
Strike (o)	225	+110	−63.8	9.4	−6.6	−55.2	94.4	19.7	−0.3	1.3	0.2
	270	+155	−46.2	40.7	−2.7	−69.9	62.5	−12.2	−0.6	0.4	−0.1
Vert. disp. (m)	2.0	+0.26	−1.8	2.3	0.2	−7.4	74.0	25.0	0.0	1.8	0.4
Focal depth (km)	11.1	−0.9	−0.1	0.1	0.0	−1.8	5.5	1.2	0.0	0.1	0.0
	20	+8.0	−2.0	1.3	−0.4	−37.9	7.1	−11.2	−1.1	0.1	−0.2
Mag	7.1	−0.4	−19.6	19.8	0.2	−76.2	−35.0	−62.1	−2.0	0.0	−0.5
	8.0	+0.5	−55.4	34.6	−4.7	33.4	470.9	208.4	−0.6	12.5	2.88
	8.5	+1.0	−66.8	18.6	−14.7	101.5	1982.9	861.9	12.4	37.2	33.5
SLR 45 (cm)	37.50	+37.5	−7.8	9.7	−0.4	−25.9	37.3	6.1	0.7	35.4	8.6
	90.60	+90.6	−29.5	29.8	0.3	−19.0	77.0	13.9	1.2	86.5	20.6
SLR 85 (cm)	55.60	+55.6	−11.4	10.1	−0.8	−21.5	65.3	9.6	1.1	66.4	12.0
	112.80	+112.8	−30.1	30.9	0.6	−35.6	101.4	15.1	2.4	85.0	24.7

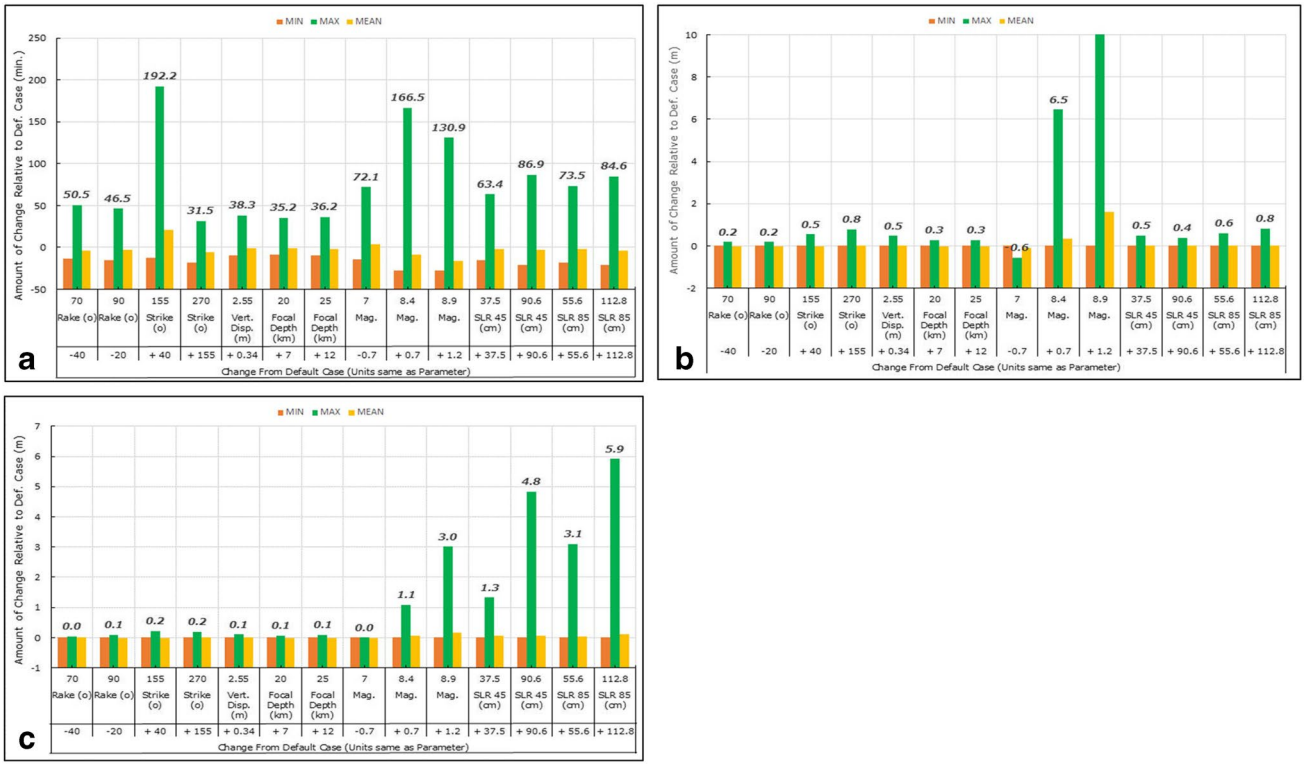

Fig. 14 **a** Sensitivity or variability analysis for ETA due to change in source parameters for 142 CE reference case; **b** sensitivity or variability analysis for wave heights due to change in source parameters for 142 CE reference case; **c** sensitivity or variability analysis for inundation depths to due to change in source parameters for 142 CE reference case

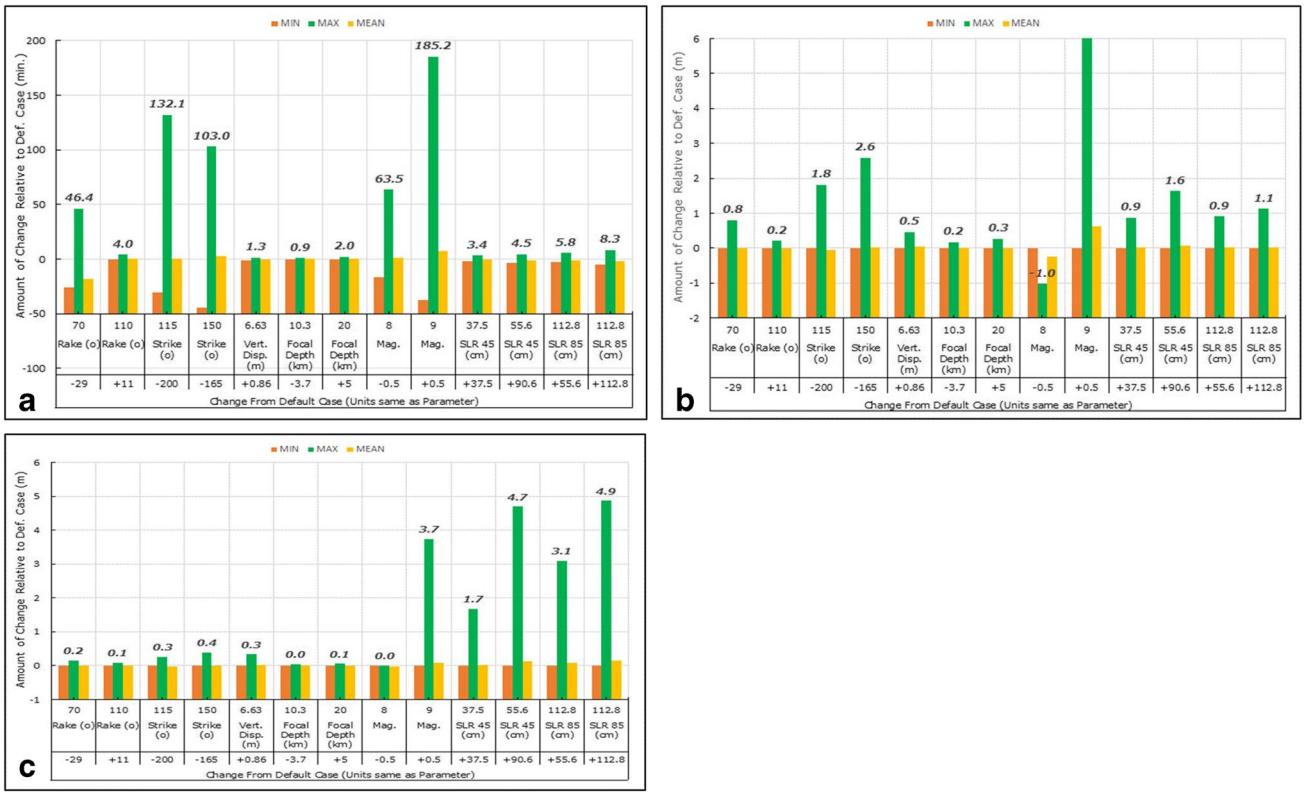

Fig. 15 **a** Sensitivity or variability analysis for ETA due to change in source parameters for 365 CE reference case; **b** sensitivity or variability analysis for wave heights due to change in source parameters for 365 CE reference case; **c** sensitivity or variability analysis for inundation depths to due to change in source parameters for 365 CE reference case

noticed in all scenarios as a rule of thumb. Our findings coincide with Yolsal and Taymaz (2010), who show that the dip and rake angles are highly dominant parameters that govern the leading tsunami waves (Tables 10, 11, 12 and Figs. 14, 15, 16 a, b, c).

Also, our results indicate that a slight increase of 13–15% in fault displacement might lead to a moderate/significant increase in wave heights, an average decrease in arrival times, and minimal effect on inundation depth (max was > 10% in case 1303 CE). This finding again coincides with Yolsal and Taymaz (2010), whose simulation displayed growing tsunami wave heights with increasing vertical displacements, as expected from theory (Tables 10–12 and Figs. 14, 15, 16 a, b, c).

Yolsal and Taymaz (2010) implemented sensitivity analysis to ascertain the influence of earthquake source parameters on tsunami generation and wave for the tsunamigenic earthquake of 1303 CE. Using different values of 5 km, 10 km, and 20 km as focal depth in their simulations while maintaining other parameters, they presented that focal depth has a significant effect on tsunami wave properties in the far-field. We concur with the above findings the decrease in focal depth result in higher wave heights, shorter arrival times, and more inundation were observed. Additionally, tsunami wave amplitude was reduced by two when focal depth lowered from 20 to 100 km.

The effect of SLR, the Delta subsidence models, storm surge, and tidal level have been discussed separately in many reviews before, but never all together in combination with tsunami as per the author's current knowledge, especially in the Egyptian-Mediterranean coastal zone of interest.

Conclusions

It is standard to study tsunami events separately, one single scenario for each event, which may lead to inaccurate results if inferred in the work of risk mitigation measures and measures. Therefore, considering a single scenario in hazard estimation does not reflect the whole reality where different seismological and source rupture parameters or source models to describe each tsunamigenic earthquake. Variability

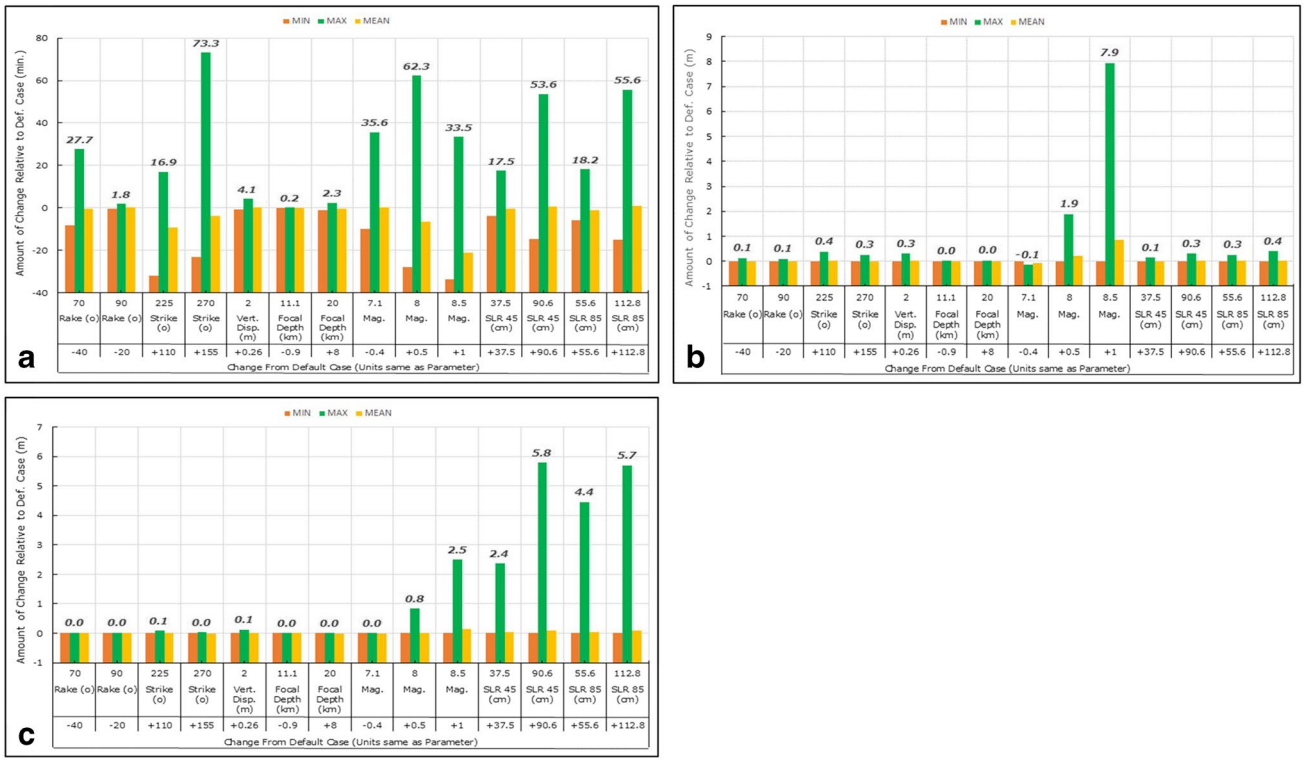

Fig. 16 **a** Sensitivity or variability analysis for ETA due to change in source parameters for 1481 CE reference; **b** sensitivity or variability analysis for wave heights due to change in source parameters for 1481 CE reference case; **c** sensitivity or variability analysis for inundation depths to due to change in source parameters for 1481 CE reference case

in seismic source parameters reflects the level of cognitive uncertainty that exists because most of these tsunamis, if not all, occurred in the pre-instrumental period. Therefore, in this work, we synthesized a set of reference and hypothetical scenarios based on the source models developed in previous works and seismotectonic knowledge of the area of influence. We also collected the topo-bathymetry information available to make a simulation on the scale of the Egyptian Northern Coastal zone. Finally, multi-scenario tsunami hazard maps, tables, and charts are presented in maps and tables for wave heights, inundation depth considering the SLR and the Delta subsidence models, and estimated arrivals, which could contribute to the development of risk reduction strategies and a national tsunami warning system.

Comparisons were made between the results calculated in this study and those from previous studies. Comparative analysis of results from this work and those obtained in previous works indicates differences in wave heights and ETAs at the sites of interests (Hamouda 2006, 2010b). This disagreement could be attributed to using an extrapolated bathymetric grid by the previous studies interests (Hamouda 2006, 2010b). Further effort is exerted to estimate tsunami wave propagation in the Rosetta promontory and the Suez Canal sites of interest. These two locations are chosen due to their strategic importance.

Tsunami hazard parameters of interest have been prepared for the hypothetical scenarios and the change in the water height, inundation depth, and estimated time of arrivals values due to the variability in the magnitude, location, and geometry of a fault. Also, temporally based scenarios such as the sea-level rise and delta sinking were considered.

The results of this investigation provide the decision-makers and other potential users with a detailed evaluation of the tsunami hazard, which in turn could assist in the development of an efficient hazard mitigation strategy or even an early warning system.

The main aims and findings comply with the Sendai Framework of action (2015–2030), e.g., understanding tsunami risk strengthening disaster risk governance to manage disaster risk, which leads to enhancing disaster preparedness for effective response and resilience. Also, this work's outcomes are considered an essential step toward achieving priorities of the National Strategy for Disaster Risk Reduction 2030.

In the end, we would like to convey that making a unified map to include all possible scenarios is more logical and accurate than adopting a single scenario for each source or event separately and is given to the reader and the decision-maker regarding the discrepancy and

uncertainty in the results. However, it is worth noting that a detailed site-specific analysis for strategic sites and mega projects within the Egyptian-Mediterranean coastal zone that adopts fine topographic/bathymetric data is indispensible.

Acknowledgements We are grateful to the Editor Dr. Abdullah M. Al-Amri and the anonymous reviewers for their careful reading of our manuscript and their insightful comments and suggestions. We are grateful to Prof. Giuliano Panza for his valuable comments and fruitful discussions. Also, the authors are grateful to Professor Ahmet Yalçıner and the team who developed the NAMI DANCE code for providing their user-friendly tsunami simulation package, with which the results of this study were obtained. A most profound appreciation to Professor Xiaoming Wang, a leading Tsunami Scientist at the GNS Science Institute for providing his support and helpful feedback in addition to the most helpful Tsunami simulation code COMCOT (Cornell Multi-Grid Coupled Tsunami Model). This research was conducted in Japan under cover of the ABE Initiative (African Business Youth Education) provided by the government of Japan; the initiative was first exposed to the general public at the 5th Tokyo International Conference on African Development (TICAD V), held in Yokohama in 2013. This work was financially supported by the Strategic Research Foundation Grant-aided Project for Private universities from the Ministry of Education (Tomoya Shibayama, Waseda University, No. S1311028).

Data Availability Data is available on request due to privacy/ethical restrictions.

Declarations

Conflict of interest The authors declare that they have no competing interests.

References

Abdelaal HSA, Thilmany D (2019) Grains production prospects and long run food security in Egypt. Sustainability 11(16):4457

Ambraseys NN (1962) Data for the investigation of the seismic sea-waves in the Eastern Mediterranean. Bull Seismol Soc Am 52(4):895–913

Ambraseys N, Synolakis C (2010) Tsunami catalogs for the Eastern Mediterranean, revisited. J Earthq Eng 14(3):309–330

Antonopoulos J (1979) Catalogue of tsunamis in the Eastern Mediterranean from antiquity to present times. Ann Geophys 32(1):113–130

Atwater BF, Cisternas MV, Bourgeois J, Dudley WC, Hendley JW, Stauffer PH (1999) Surviving a tsunami-lessons from Chile, Hawaii, and Japan. US Geol Surv Circ 1187:1–19

Becker JJ, Sandwell DT, Smith WHF, Braud J, Binder B, Depner JL, ... Weatherall P (2009) Global bathymetry and elevation data at 30 arc seconds resolution: SRTM30_PLUS. Mar Geod 32(4): 355–371

Becker RH, Sultan M (2009) Land subsidence in the Nile Delta: inferences from radar interferometry. The Holocene 19(6):949–954

Ben-Menahem S (1979) Confinement in compact QED for low couplings. Phys Rev D 20(8):1923

Briais A, Singh SC, Tapponnier P, Elias A, Sursock A, Jomaa R, ... Jacques E (2004) Neogene and active shortening offshore the reactivated Levant margin in Lebanon: results of the SHALIMAR cruise, vol 2004. In AGU Fall Meeting Abstracts, San Francisco, pp T53B-0490

Chow GC (1960) Tests of equality between sets of coefficients in two linear regressions. Econometrica: J Econom Soc 28:591–605

CORI (1992) Vulnerability assessment to accelerated sea level rise; Case Study Egypt.: Coastal Research Institute

DeMets C, Iaffaldano G, Merkouriev S (2015) High-resolution Neogene and quaternary estimates of Nubia-Eurasia-North America plate motion. Geophys J Int 203(1):416–427

Dong L, Tong X, Ma J (2021) Quantitative investigation of tomographic effects in abnormal regions of complex structures. Engineering 7(7):1011–1022

El-Asmar HM, Hereher ME (2011) Change detection of the coastal zone east of the Nile Delta using remote sensing. Environ Earth Sci 62(4):769–777

Elias A, Tapponnier P, Singh SC, King GC, Briais A, Daëron M, ... Klinger Y (2007) Active thrusting offshore Mount Lebanon: source of the tsunamigenic AD 551 Beirut-Tripoli earthquake. Geology 35(8):755–758

El-Raey M, Fouda Y, Nasr S (1997) GIS assessment of the vulnerability of the Rosetta area, Egypt to impacts of sea rise. Environ Monit Assess 47(1):59–77

El-Raey M (2010) Impact of sea level rise on the Arab Region. University of Alexandria. Arab Academy of Science, Technology, and Maritime. https://www.researchgate.net/publication/266454174_Impact_of_Sea_Level_Rise_on_the_Arab_Region

El-Sayed A, Romanelli F, Panza G (2000) Recent seismicity and realistic waveforms modeling to reduce the ambiguities about the 1303 seismic activity in Egypt. Tectonophysics 328(3-4):341–357

Ericson JP, Vörösmarty CJ, Dingman SL, Ward LG, Meybeck M (2006) Effective sea-level rise and deltas: causes of change and human dimension implications. Glob Planet Chang 50(1–2):63–82

Freitag HP, McPhaden MJ, Cronin MF, Sabine CL, McClurg DC, McLain PD (2006) PMEL contributions to the OceanSITES program. In OCEANS 2006, IEEE, Boston, pp 1–6. https://doi.org/10.1109/OCEANS.2006.307077

Frihy OES, Deabes EA, Shereet SM, Abdalla FA (2010) Alexandria-Nile Delta coast, Egypt: update and future projection of relative sea-level rise. Environ Earth Sci 61(2):253–273

Galanopoulos AG (1960) Tsunamis observed on the coasts of Greece from antiquity to present time. Ann Geofis 13(3–4):369–386

Hamouda AZ (2006) Numerical computations of 1303 tsunamigenic propagation towards Alexandria, Egyptian coast. J Afr Earth Sci 44(1):37–44

Hamouda AZ (2010a) A reanalysis of the AD 365 tsunami impact along the Egyptian Mediterranean coast. Acta Geophysica 58(4):687

Hamouda AZ (2010b) Worst scenarios of tsunami effects along the Mediterranean coast of Egypt. Mar Geophys Res 31:197–214. https://doi.org/10.1007/s11001-010-9099-4

Hassan HM, Frischknecht C, ElGabry MN, Hussein H, ElWazir M (2020) Tsunami hazard and risk assessment for Alexandria (Egypt) based on the maximum credible earthquake. J Afr Earth Sc 162:103735

Jol A, Raes F, Menne B (2009) Impacts of Europe's changing climate–2008 indicator-based assessment. In IOP Conference Series. Earth and Environmental Science (vol 6, No 29). IOP Publishing, Bristol

Ma J, Dong L, Zhao G, Li X (2018) Discrimination of seismic sources in an underground mine using full waveform inversion. Int J Rock Mech Min Sci 106:213–222

Ma J, Dong L, Zhao G, Li X (2019) Focal mechanism of mining-induced seismicity in fault zones: a case study of yongshaba mine in China. Rock Mech Rock Eng 52(9):3341–3352

Masria A, Negm AM, Iskander M (2016) Assessment of nile delta coastal zone using remote sensing. In: Negm A (eds) The Nile Delta. The Handbook of Environmental Chemistry, vol 55. Springer, Cham. https://doi.org/10.1007/698_2016_55

Mitsoudis DA, Flouri ET, Chrysoulakis N, Kamarianakis Y, Okal EA, Synolakis CE (2012) Tsunami hazard in the southeast Aegean Sea. Coast Eng 60:136–148

Okada Y (1985) Surface deformation due to shear and tensile faults in a half-space. Bull Seism Soc Am 75:1135–1154

Panza GF, Bela J (2020) NDSHA: A new paradigm for reliable seismic hazard assessment. Eng Geol 275:105403

Papadopoulos GA (2003) Tsunami hazard in the Eastern Mediterranean: strong earthquakes and tsunamis in the Corinth Gulf, Central Greece. Nat Hazards 29(3):437–464

Papadopoulos GA, Chalkis BJ (1984) Tsunamis observed in Greece and the surrounding area from antiquity up to the present times. Mar Geol 56(1–4):309–317

Papadopoulos GA, Fokaefs A (2005) Strong tsunamis in the Mediterranean Sea: a re-evaluation. ISET J Earthq Technol 42(4):159–170

Papadopoulos GA, Daskalaki E, Fokaefs A, Giraleas N (2007) Tsunami hazards in the Eastern Mediterranean: strong earthquakes and tsunamis in the East Hellenic Arc and Trench system. Nat Hazards Earth Syst Sci 7(1):57–64

Papadopoulos GA, Gràcia E, Urgeles R, Sallares V, De Martini PM, Pantosti D, ... Papageorgiou A (2014) Historical and pre-historical tsunamis in the Mediterranean and its connected seas: geological signatures, generation mechanisms and coastal impacts. Mar Geol 354:81–109. https://doi.org/10.1016/j.margeo.2014.04.014

Rugarli P, Vaccari F, Panza G (2019) Seismogenic nodes as a viable alternative to seismogenic zones and observed seismicity for the definition of seismic hazard at regional scale. https://doi.org/10.48550/arXiv.1902.02108

Salama A, Meghraoui M, El Gabry M, Maouche S, Hussein MH, Korrat I (2018) Paleotsunami deposits along the coast of Egypt correlate with historical earthquake records of eastern Mediterranean. Nat Hazard 18(8):2203–2219

Shah-Hosseini M, Saleem A, Mahmoud AMA, Morhange C (2016) Coastal boulder deposits attesting to large wave impacts on the Mediterranean coast of Egypt. Nat Hazards 83(2):849–865

Shaltout M, Tonbol K, Omstedt A (2015) Sea-level change and projected future flooding along the Egyptian Mediterranean coast. Oceanologia 57(4):293–307

Shuto N, Goto C, Imamura F (1990) Numerical simulation as a means of warning for near field tsunamis. Coast Eng Japan 33(2):173–193. https://doi.org/10.1080/05785634.1990.11924532

Shuto N, Goto C, Imamura F (1991) Numerical simulation as a means of warning for near field tsunamis. In: Brennan AN, Lander JF (eds) 2nd UJNR Tsunami Workshop Proceedings. National Geophysical Data Center, Boulder Colorado, pp 133–153

Soloviev SL, Solovieva ON, Go CN, Kim KS, Shchetnikov NA (2000) Tsunamis in the Mediterranean Sea 2000 BC-2000 AD, vol 13. Springer Science & Business Media, Dordrecht, p 256

Stanley DJ (1990) Recent subsidence and northeast tilting of the Nile delta, Egypt. Mar Geol 94(1–2):147–154

Tinti S, Armigliato A, Pagnoni G, Zaniboni F (2005) Scenarios of giant tsunamis of tectonic origin in the Mediterranean. ISET J Earthq Technol 42(4):171–188

Tinti S, Maramai A (1996) Catalogue of tsunamis generated in Italy and in Cote d'Azur, France: a step towards a unified catalogue of tsunamis in Europe. Ann Geofis 39:1253–1299

Torab M, Dalal N (2015) Natural hazards mapping of mega sea waves on the NW coast of Egypt. J Afr Earth Sci 112:353–357. https://doi.org/10.1016/j.jafrearsci.2015.09.022

Valle BL, Kalligeris N, Findikakis AN, Okal EA, Melilla L, Synolakis CE (2014) Plausible megathrust tsunamis in the eastern Mediterranean Sea. Proc Inst Civ Eng-Eng Comput Mech 167(3):99–105

Wang X, Power W (2011) COMCOT: a tsunami generation, propagation and run-up model. GNS Science Report, 2011/43, GNS Science, Lower Hutt, New Zealand, pp 121

Warne AG, Stanley DJ (1993) Archaeology to refine Holocene subsidence rates along the Nile delta margin, Egypt. Geology 21(8):715–718

Weatherall P (2009) Global bathymetry and elevation data at 30 arc seconds resolution: SRTM30_PLUS. Mar Geod 32(4):355–371

Woodward J (ed) (2020) The physical geography of the mediterranean. Oxford Academic, Oxford. https://doi.org/10.1093/oso/9780199268030.001.0001

Yalciner AC, Pelinovsky E, Zaytsev A, Chernov A, Kurkin A, Ozer C, Karakus H (2006) Nami dance manual, METU. Civil Engineering Department, Ocean Engineering Research Center, Ankara, Turkey

Yalciner AC, Zahibo N, Pelinovsky E, Insel I, Dilmen DI, Zaytsev A, ... Ozer C (2010) Understanding the Possible Effects of Near and Far Field Tsunamis on Lesser Antilles by Numerical Modeling. Open Oceanogr J 4:50–57. https://doi.org/10.2174/1874252101004010050

Yolsal S, Taymaz T (2010) Sensitivity analysis on relations between earthquake source rupture parameters and far-field tsunami waves: case studies in the Eastern Mediterranean Region. Turk J Earth Sci 19(3):313–349

Zaytsev A, Kurkin A, Pelinovsky E, Yalciner AC (2019) Numerical tsunami model nami-dancE. Sci Tsunami Haz 38(4):151. http://tsunamisociety.org/384ZaytsevEtAl.pdf